Available online at www.sciencedirect.com
SCIENCE DIRECT®
Journal of Computational Physics 201 (2004) 685–722
JOURNAL OF COMPUTATIONAL PHYSICS
www.elsevier.com/locate/jcp

A surfactant-conserving volume-of-fluid method for interfacial flows with insoluble surfactant

Ashley J. James [a,*], John Lowengrub [b]

[a] Department of Aerospace Engineering and Mechanics, University of Minnesota, 107 Akerman Hall, 110 Union St SE, Minneapolis 55455, USA
[b] Department of Mathematics, University of California, Irvine

Received 1 March 2004; received in revised form 15 June 2004; accepted 23 June 2004
Available online 13 August 2004

Abstract

An axisymmetric numerical method to simulate the dynamics of insoluble surfactant on a moving liquid–fluid interface is presented. The motion of the interface is captured using a volume-of-fluid method. Surface tension, which can be a linear or nonlinear function of surfactant concentration (equation of state), is included as a continuum surface force. The surfactant evolution is governed by a convection–diffusion equation with a source term that accounts for stretching of the interface. In the numerical method, the masses of the flow components and the surfactant mass are exactly conserved. A number of test cases are presented to validate the algorithm. Simulations of a drop in extensional flow, and its subsequent retraction and breakup upon cessation of the external flow, are performed. Even when the initial surfactant distribution is dilute, we observe that increases in surfactant concentration locally (i.e. at the drop tips) can result in a local deviation from the dilute limit. We show that this can lead to differences in effective surface tension, the Marangoni forces and the associated drop dynamics between results using the linear and nonlinear equations of state.

Keywords: Surfactant; VOF; Interfacial flow; Surface tension

1. Introduction

Surfactant plays a critical role in numerous important industrial and biomedical applications. For example, the formation of very small drops or bubbles by tip streaming relies on the presence of surfactant [1]. The production of such tiny droplets is useful in drug delivery, industrial emulsification [2], liquid/liquid

* Corresponding author. Tel.: +1-612-625-6027; fax: +1-612-626-1558.
E-mail addresses: ajames@aem.umn.edu (A.J. James), lowengrb@math.uci.edu (J. Lowengrub).

0021-9991/$ - see front matter © 2004 Elsevier Inc. All rights reserved.
doi:10.1016/j.jcp.2004.06.013

extraction and hydrodesulfurization of crude oil [3], polymer blending and plastic production [4], and other applications.

Surfactants adhere to interfaces resulting in a lowered, non-uniform surface tension along the interface. This makes the capillary force non-uniform and introduces the Marangoni force. Further, there may be exchange (adsorption/desorption) of surfactants between the interface and the bulk [2]. Interfacial surfactant is transported with the interface by convection, and may diffuse along the interface in the presence of a surfactant concentration gradient. Additionally, compression or stretching of the interface causes a corresponding increase or decrease in the concentration. The equation that governs these dynamics has been derived in various forms in [5,6] and is derived in Appendix A in an alternate form that we use here. The motion of the surfactant and of the surrounding bulk fluids are coupled through the Marangoni force.

While there have been many numerical studies of clean, deformable interfaces, there have been few studies that incorporate the effects of surfactants. In axisymmetric Stokes flows, Stone and Leal [7] investigated the effect of insoluble surfactant on drop-breakup. Milliken et al. [8] investigated the effects of the drop/matrix viscosity ratio and the nonlinear equation of state relating the surface tension to the surfactant concentration. Pawar and Stebe [9] investigated the effects of interfacial saturation and interaction. Eggleton et al. [10] further investigated the effect of the nonlinear equation of state and finally Eggleton et al. [11] used boundary integral methods to investigate the onset of tip streaming. In fully 3D flows, Li and Pozrikidis [12] and Yon and Pozrikidis [13] investigated the effects of insoluble surfactant on drop dynamics in Stokes flows using boundary integral methods. Solubility effects were considered in Stokes flows by Milliken and Leal [14] for axisymmetric drop dynamics and very recently by Zhou et al. [15] for drop–drop interactions and coalescence in 3D. The latter work utilized a sharp-interface finite element approach.

Continuum formulations of the governing sharp interface equations have been implemented numerically primarily for clean drops although there has been recent work on surfactants by Jan and Tryggvason [16] who studied the effect of surfactants on rising bubbles using an immersed boundary/front tracking method and Ceniceros [17] who used a hybrid level-set/front tracking method to study the effect of surfactants on capillary waves. Xu and Zhao [52] presented a methodology to simulate surfactant transport on a deformable interface in conjunction with a level set method. They did not couple their method to a flow solver, but presented several test cases in which a velocity field is prescribed (they reported up to 6% loss of total surfactant mass). Very recently, Renardy and co-workers [34,51] presented simulations of 3D drops with surfactant using the volume-of-fluid method (described further below). This work thus far has been limited to assuming a linear relation between the surfactant concentration and surface tension (equation of state). In our method, we allow an arbitrary equation of state.

Continuum approaches to simulating interface dynamics include immersed-boundary/ front-tracking (e.g. see [18–22]), level set (e.g. [23–25]), phase-field (e.g. [28–33]), volume-of-fluid (VOF) (e.g. [34–42,55,56]), coupled level-set and volume of fluid [43–45], immersed interface (e.g. see [48,49,26,27]) and ghost-fluid (e.g. [46,47]) methods. In the latter two methods, the interface jump conditions are handled explicitly by modifying the difference stencils near the interface in various ways. In all of the other methods, the flow discontinuities (density, viscosity) are smoothed and the surface tension force is distributed over a thin layer near the interface to become a volume force. As the thickness of the layer approaches zero the volume force approaches the proper surface force. The Navier–Stokes equations are then solved on a fixed Eulerian mesh making the extension to 3D straightforward. Each method differs in the details of how this is carried out.

The volume of fluid (VOF) method was developed by [42] and [55] and is the method we use in this paper. The main advantages of the method are that the interface shape is not constrained, changes in topology are handled automatically, and mass of each flow component is conserved exactly. The interface location is captured as it moves through the grid by tracking the local volume fraction. The volume fraction is constant in each fluid and discontinuous at the interface. The volume fraction convection equation is solved in every cell, but is nontrivial only near an interface. To maintain the discontinuous nature of the volume

fraction care is taken not to introduce numerical diffusion when solving the equation. Numerical diffusion would cause smoothing of the discontinuity and the interface would become smeared normal to itself. The approach used to avoid this is to calculate the flux of one of the fluids across each cell face using a reconstruction of the interface position. The fluxes are then used to update the volume fraction to the next time step.

As mentioned previously, Renardy et al. [34] have recently developed a VOF method for 3D drop deformation in the presence of insoluble surfactants. To our knowledge, this was the first application of a continuum-based method to study surfactant dynamics. We note that tangential surface forces due to variable surface tension had also previously been implemented in a 2D VOF method for temperature gradient driven Marangoni convection in a cavity [50]. The implementation of surfactant in [34] was somewhat ad hoc and only surfactants with linear equations of state were considered. This method was applied to study drop deformation in shear flows in 3D. It was found that when the drop becomes cusp-like, the simulation becomes sensitive to the discretization parameters and the surfactant can diffuse off the drop surface. Although the simulations appear to show tip streaming, the surfactant concentration becomes very high at the drop tips and the surface tension actually becomes negative. A mesh refinement study indicated that the results depend on the temporal and spatial step sizes. More recently, Drumright-Clarke and Renardy [51] used this algorithm to examine the effect of surfactant on the critical conditions for 3D drop break-up in shear flow.

In the current paper we present a numerical method that incorporates surfactant dynamics in an axisymmetric, incompressible Navier–Stokes solver based on the VOF method for interface capturing. We focus on the case of insoluble surfactant and the surfactant mass is exactly conserved along the interface by our algorithm. An arbitrary equation of state relating the surfactant concentration to the surface tension may be used. A number of test cases are presented to validate the algorithm. Simulations of a drop in extensional flow, and its subsequent retraction and breakup upon cessation of the external flow, are performed. Even when the initial surfactant distribution is dilute, we observe that increases in surfactant concentration locally (i.e. at the drop tips) can result in a local deviation from the dilute limit. We show that this can lead to differences in effective surface tension, Marangoni forces and the associated drop dynamics between results using the linear and nonlinear equations of state.

The remainder of this paper is organized as follows. In Section 2 we present the governing equations. In Section 3 we describe the numerical method used for the interface evolution, the surfactant evolution and the surface tension force. In Section 4 we present a series of simulations used to validate the numerical method. Section 5 is dedicated to conclusions and future work.

2. Governing equations

We assume that the flow is incompressible in both fluids, so the velocity, $\underline{u}$, is divergence free, $\nabla\cdot\underline{u} = 0$. The volume of fluid (VOF) method is used to track the interface between the two fluids, called fluid 1 and fluid 2. In this method a volume fraction, F, is defined in each grid cell as the fraction of the cell that contains fluid 1. Here we assume that $F = 1$ in the region interior to the interface. The volume fraction evolution is governed by a convection equation that ensures the interface moves with the velocity of the fluid

$$\frac{\partial F}{\partial t} + \underline{u}\cdot\nabla F = 0. \tag{1}$$

Surface tension is included via the continuum surface force (CSF) method (e.g. [54]). The CSF is included in the momentum equation, so the momentum equation satisfies the stress balance boundary condition on the interface. The surface tension force is calculated in every cell, but it is nonzero only near the interface. Using the VOF and CSF methods makes it unnecessary to apply boundary conditions at the interface

and one set of governing equations applies to the entire domain (cells containing only fluid 1, cell containing only fluid 2, and cells containing an interface). Since the same equations are solved in the whole domain the density and viscosity must be retained as variables in the momentum equation even though they are both constant in each fluid. In interfacial cells the density and viscosity are computed as linear functions of the volume fraction. The equations are non-dimensionalized with length scale L, velocity scale U, inertial time and pressure scales, and surface tension scale σ_{eq}, which is the equilibrium surface tension (the surface tension corresponding to a uniformly distributed surfactant with equilibrium concentration Γ_{eq}). The density and viscosity are scaled by the properties of fluid 1 and for simplicity we assume graviational forces are negligible. Thus, the momentum equation becomes

$$\rho\left(\frac{\partial \underline{u}}{\partial t}+\underline{u}\cdot\nabla\underline{u}\right)=-\nabla p+\frac{1}{Re}\nabla\cdot[\mu(\nabla\underline{u}+\nabla\underline{u}^{\mathrm{T}})]+\frac{1}{Re\,Ca}\underline{F}_{\mathrm{S}}, \tag{2}$$

where ρ is the density, p is the pressure, $Re=\rho_1 U\,L/\mu_1$ is the Reynolds number, μ is the viscosity and $Ca=U\mu_1/\sigma_{\mathrm{eq}}$ is the capillary number. The surface force $\underline{F}_{\mathrm{S}}$ is

$$\underline{F}_{\mathrm{S}}=\nabla\cdot[\sigma(\underline{\underline{I}}-\underline{n}\underline{n})\delta_\Sigma]=-\sigma\kappa\delta_\Sigma\underline{n}+\frac{\partial\sigma}{\partial s}\delta_\Sigma\underline{s}, \tag{3}$$

where σ is the surface tension, $\underline{n}$ is the unit vector normal (outward) to the interface, δ_Σ is the surface delta function, κ is the interface curvature and $\underline{s}$ is the unit vector tangent to the interface in the s direction. The first term on the right-hand side of Eq. (3) is the capillary force and the second term is the Marangoni force.Additionally a density ratio, $\alpha=\rho_1/\rho_2$, and a viscosity ratio, $\lambda=\mu_1/\mu_2$, are defined. The normal vector and the surface delta function are determined from the gradient of the volume fraction,

$$\underline{n}=-\frac{\nabla F}{|\nabla F|},\qquad \delta_\Sigma=|\nabla F|. \tag{4}$$

The surfactant concentration evolution is governed by a convection–diffusion equation with a source term to account for interfacial stretching,

$$\frac{\partial\Gamma}{\partial t}+\underline{u}\cdot\nabla\Gamma=\frac{1}{Pe_{\mathrm{S}}}\nabla_{\mathrm{S}}^2\Gamma+\Gamma\underline{n}\cdot\nabla\underline{u}\cdot\underline{n}, \tag{5}$$

where Γ is the interfacial surfactant concentration, scaled by the equilibrium concentration, Γ_{eq}, $Pe_{\mathrm{S}}=UL/D_{\mathrm{S}}$ is the surface Peclet number, D_{S} is the surface diffusivity of surfactant, and ∇_{S}^2 is the surface Laplacian operator. To see that Eq. (5) is well defined and is equivalent to alternative formulations of the surfactant equation (e.g. [5,6]), see Appendix A.

In our finite volume method, we do not solve Eq. (5) directly and instead relate the surfactant concentration (in a finite volume) to the ratio of the surfactant mass M and surface area A in that volume, i.e.

$$\Gamma=\frac{M}{A}. \tag{6}$$

The surfactant mass and surface area are tracked independently as described below.

The area has been non-dimensionalized by L^2 and the mass by $\Gamma_{\mathrm{eq}}L^2$. Siegel [63] has also proposed decomposing concentration into mass and area. The equations for M and A are derived as follows. The interfacial area in a finite volume, V, is obtained by integrating the surface delta function over the volume

$$A=\int_{\mathrm{V}}\delta_\Sigma\,\mathrm{d}V. \tag{7}$$

Integrating the concentration times the surface delta function over the volume yields the surfactant mass,

$$M = \int_{\mathrm{V}} \Gamma \delta_\Sigma \, \mathrm{d}V. \tag{8}$$

Differentiation of Eq. (7) with respect to time yields

$$\frac{\mathrm{D}A}{\mathrm{D}t} = -\int_{\mathrm{V}} (\underline{n} \cdot \nabla \underline{u} \cdot \underline{n}) \delta_\Sigma \, \mathrm{d}V. \tag{9}$$

The left-hand side of Eq. (9) is the time rate of change of the area of a material element of the interface. The right-hand side represents changes in interfacial area due to stretching. For a vanishing volume, this can be written in differential form as

$$\frac{\mathrm{D}A}{\mathrm{D}t} = \frac{\partial A}{\partial t} + \underline{u} \cdot \nabla A = -A(\underline{n} \cdot \nabla \underline{u} \cdot \underline{n}), \tag{10}$$

which is also derived by Batchelor [53]. The mass of surfactant on a material element of the interface can change if there is diffusion along the interface. Diffusion of mass through the boundary of a finite volume occurs through the curve where the interface intersects the boundary. A segment of this curve, called C, is illustrated in Fig. 1. Using Fick's Law of mass diffusion, the mass is governed by

$$\frac{\mathrm{D}M}{\mathrm{D}t} = \frac{1}{Pe_{\mathrm{S}}} \int_{\mathrm{C}} (\underline{n} \times \hat{n}_{\mathrm{V}} \times \underline{n}) \cdot \nabla_{\mathrm{S}} \Gamma \, \mathrm{d}C, \tag{11}$$

where $\hat{n}_{\mathrm{V}}$ is the unit vector pointed normally outward to the boundary of the volume. The cross product $\underline{n} \times \hat{n}_{\mathrm{V}}$ gives the direction tangent to both the interface and the cell, along C. Mass diffused in this direction along the interface does not cross the boundary of the finite volume. The cross product $\underline{n} \times \hat{n}_{\mathrm{V}} \times \underline{n}$ gives the other portion of the diffusion that is tangent to the interface and that does cross the boundary of the volume. Thus, the right-hand side of Eq. (11) is obtained.

Using the divergence theorem, Eq. (11) can be written as

$$\frac{\mathrm{D}M}{\mathrm{D}t} = \frac{1}{Pe_{\mathrm{S}}} \int_{\mathrm{V}} \nabla_{\mathrm{S}}^2 \Gamma \delta_\Sigma \, \mathrm{d}V. \tag{12}$$

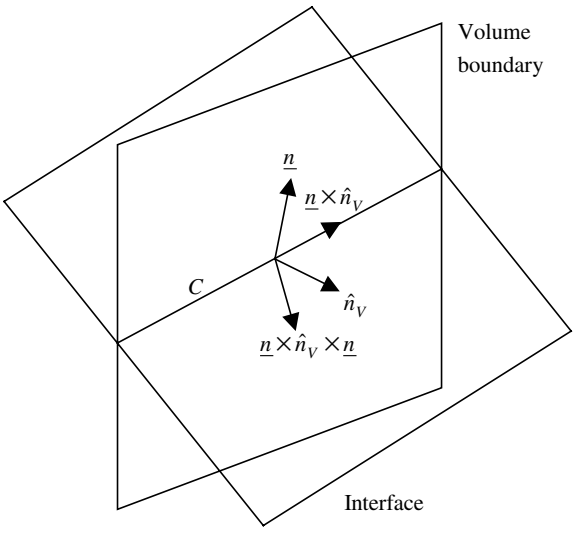

Fig. 1. Interface geometry used in evaluating interfacial diffusion of surfactant mass.

This leads to a differential form for a vanishing volume

$$\frac{\mathrm{D}M}{\mathrm{D}t} = \frac{\partial M}{\partial t} + \underline{u} \cdot \nabla M = \frac{A}{Pe_{\mathrm{S}}} \nabla_{\mathrm{S}}^2 \Gamma. \tag{13}$$

Eq. (5) is regained by combining Eqs. (6), (10) and (13).

Finally, an equation of state is given for the surface tension as a function of surfactant concentration. In this method the equation of state may be linear or nonlinear. For example, the Langmuir equation of state is

$$\sigma = \frac{1 + E \ln(1 - x\Gamma)}{1 + E \ln(1 - x)}, \tag{14}$$

where E is the surfactant elasticity and $x = \Gamma_{\mathrm{eq}}/\Gamma_*$ is a measure of surfactant coverage; Γ_* is the concentration of the surfactant in the maximum packing limit. A linear equation of state can also be used:

$$\sigma = 1 + \beta(1 - \Gamma), \tag{15}$$

where $\beta = Ex$ in the limit of small x. Note that for both equations of state the scaling is constructed so that the equilibrium dimensionless concentration, $\Gamma = 1$, corresponds to the equilibrium dimensionless surface tension, $\sigma = 1$.

3. Computational method

3.1. Introduction

The axisymmetric governing equations are discretized using a finite-volume method, on a fixed, structured, uniform, staggered grid, in a rectangular domain in the r–z plane. In the staggered grid arrangement all variables except the velocity components are defined at cell centers (i,j), where index i represents a grid line of constant r and index j represents a grid line of constant z. The radial velocity component, u, is defined on $(i+\frac{1}{2}, j)$ cell faces and the vertical component, v, on $(i, j+\frac{1}{2})$ cell faces.

An explicit Euler time integration method is used, except that surfactant diffusion is discretized implicitly as described in Section 3.6. At each time step, first the velocity and pressure are updated, and then the volume fraction and the surfactant distribution are updated as described below. Adaptive time stepping is used to ensure computational stability. The time step is limited at each step by convective, viscous, and capillary criteria. These limits are parameterized by a Courant number, Δt_{C}, a von Neumann number, Δt_{vN}, and a capillary time step limit, Δt_{Cap}, such that

$$\Delta t = \min\left(\frac{\Delta t_{\mathrm{C}} \Delta x}{U_{\max}}, \Delta t_{\mathrm{vN}} Re \left(\frac{\Delta x}{2}\right)^2, \Delta t_{\mathrm{Cap}} Re\, Ca \Delta x^{3/2}\right), \tag{16}$$

where Δx is the minimum spatial step size and $U_{\max}$ is the maximum velocity component magnitude in the domain. In the results presented in Section 4, $\Delta t_{\mathrm{C}} = \Delta t_{\mathrm{vN}} = \Delta t_{\mathrm{Cap}} = 0.1$ unless otherwise specified.

Because of the convection routine used, the Courant number must be less than one to ensure that the interface does not move through more than one grid cell in a single time step. We use 0.1 as a more conservative value to ensure accuracy and stability. The use of other advection algorithms [67,68] could be used to relax this time step stability constraint.

The continuity and momentum equations are discretized using second-order central differences, except for the surface stress, which is described in Section 3.7. The explicit MAC method [57] is used to compute the velocity and pressure fields. The resulting discrete pressure-Poisson equation is solved using an incom-

plete-Cholesky conjugate-gradient method [58]. The flow solver and the volume fraction evolution algorithms, and their verification, are described in more detail in [35,59].

3.2. Basic strategy for surfactant evolution

The method used to compute the evolution of the surfactant is inspired by the VOF method. In the VOF method, the volume of fluid 1 in a grid cell at the beginning of a time step is simply the cell volume times the volume fraction, by definition. During a time step the volume of fluid 1 that moves between each pair of adjacent grid cells (the volume flux) is computed. The volume fraction at the end of a time step is then computed as the initial volume of fluid 1 minus the net volume flux out of the cell, divided by the cell volume. Thus, although Eq. (1) governs the evolution of the volume fraction, the method actually tracks fluid volumes. This is equivalent to tracking fluid masses, since the density of each fluid is constant, and ensures mass conservation.

The surfactant concentration is the mass concentration of surfactant on the interface, just as the volume fraction is the volume concentration of fluid 1 in a grid cell. The current approach to surfactant concentration evolution is analogous to volume fraction evolution in that surfactant mass is tracked. The concentration in a grid cell is then determined by dividing the surfactant mass in the cell by the surface area of the interface in the cell. Compared to the volume fraction evolution, the surfactant concentration evolution is complicated by the fact that surfactant mass may be transported between cells by diffusion as well as convection, and that the surface area in a cell may vary, unlike the cell volume. Because of this, it is critical to accurately track the surface area, as well as the volume fraction. The importance of "accuracy in the representation of the surface geometry" has also been recognized by Yon and Pozrikidis [13].

Thus, the concentration of surfactant in a grid cell can change by three mechanisms, as described by the governing equation: convection, diffusion and area stretching/compression. In practice, this is accomplished in three sub-steps during each time step. Surfactant mass and area are numerically convected in tandem with the volume fraction, since these quantities are physically convected together. Area stretching and mass diffusion are computed separately.

In the VOF method the interface is "reconstructed" at the beginning of a time step for more accurate simulation of its evolution. This reconstruction is the approximation of the interface as a line segment in each interfacial cell. This segment then defines *where* the volume of fluid 1 lies within the cell. Similarly, to accurately describe the surfactant distribution in a grid cell the concentration is reconstructed as a linear function along the interfacial line segment.

In the remainder of this section is organized as follows. The volume fraction and concentration reconstructions are described first, in Section 3.3, since they are used in computing the evolution. Next, the method used to evolve the volume fraction is reviewed in Section 3.4. Then the surface area evolution is described, Section 3.5, followed by the surfactant evolution, Section 3.6. Finally, the method used to compute the surface force is presented in Section 3.7.

3.3. Volume fraction and surfactant concentration reconstruction

To convect volumes of fluid while preventing smearing of the interface normal to itself it is first necessary to reconstruct the interface from the volume fraction field. This interface reconstruction locates where the volume of fluid 1 resides in the cell, rather than assuming both fluids are distributed uniformly. We have found that convection of surfactant similarly suffers from excessive numerical diffusion if the surfactant is assumed to uniformly distributed along the interface, so its distribution is also reconstructed. The reconstruction is illustrated in Fig. 2. The interface and the concentration are both reconstructed at the beginning of each time step and at intermediate steps as needed.

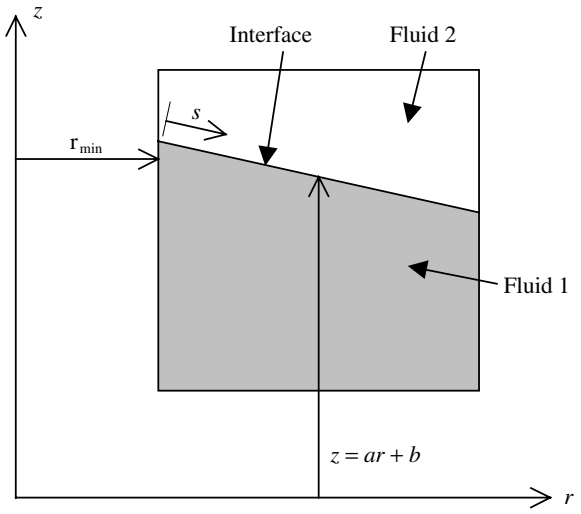

Fig. 2. Interface reconstruction. The interface is approximated by the straight line $z = ar + b$. The concentration is approximated as a linear function of the coordinate, s, along the line.

The volume fraction distribution in a cell is determined by approximating the interface in a cell as a straight line

$$z = ar + b. \tag{17}$$

Note that a straight-line approximation of the interface in the r–z plane defines a conical axisymmetric surface. The line segment approximation of the interface is defined independently in each cell, so the approximate interface need not be continuous from one cell to the next. First, the normal vector is computed as the volume fraction gradient using a finite difference method with a nine-point stencil. The normal vector defines the slope, a,

$$a = -\frac{n_r}{n_z}, \tag{18}$$

where n_r and n_z are the radial and vertical components of the normal vector, respectively. The normal vector is also used to flag whether fluid 1 resides above or below the line. The intercept, b, is calculated iteratively so that the volume of fluid 1 defined by the line divided by the cell volume equals the cell volume fraction, $F_{i,j}$.

The surfactant concentration is reconstructed as a linear function of position, s, along the straight-line interface reconstruction

$$\Gamma = (\nabla_S \Gamma)s + c, \tag{19}$$

where the surface gradient, $\nabla_S \Gamma$, is taken to be constant in each cell. As for the interface reconstruction, the function need not be continuous from one cell to the next. Since the concentration is only defined on the interface the surface gradient cannot be computed using a simple finite difference formula, as the normal vector is for the interface reconstruction. Instead the gradient is computed using only the two adjacent cells that contain an interface segment. This is illustrated in Fig. 3 for the case in which the adjacent cells that contain an interface segment are cells $(i + 1, j)$ and $(i - 1, j)$. The procedure is equivalent if other adjacent cells are used. Normally exactly two adjacent grid cells will have non-zero interfacial area, but to account for possible degeneracies the two adjacent cells with the largest interfacial areas are used. The locations of

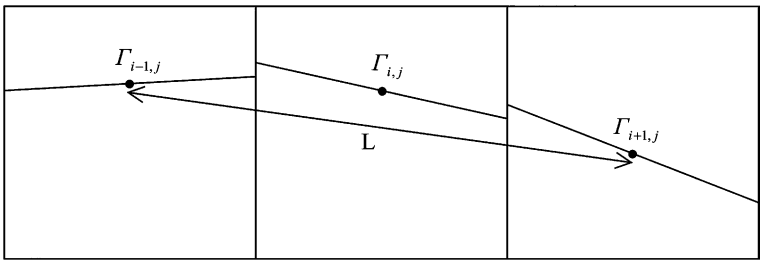

Fig. 3. Computation of surface gradient of surfactant.

the midpoints of the straight-line interface approximations in each of these cells are determined. The concentration gradient is the difference in concentration between the two cells divided by the distance, L, between their interface midpoints. For the case illustrated in Fig. 3, for example

$$(\nabla_S \Gamma)_{i,j} = \frac{\Gamma_{i+1,j} - \Gamma_{i-1,j}}{L}. \tag{20}$$

The intercept, c, in the concentration reconstruction is then computed to ensure that the average concentration defined by Eq. (19) equals the known average concentration in the cell, $\Gamma_{i,j}$. This is done by integrating the concentration over the straight line and dividing by the area of the line

$$\Gamma_{i,j} = \frac{\int_{r_{\min}}^{r_{\max}} 2\pi r \Gamma \, \mathrm{d}s}{\int_{r_{\min}}^{r_{\max}} 2\pi r \, \mathrm{d}s}. \tag{21}$$

Using Eq. (19), the relationship $s = \sqrt{1+a^2}(r - r_{\min})$, where $r_{\min}$ is the radial location of the interface endpoint where the coordinate s originates and $\mathrm{d}s = \sqrt{1+a^2}\,\mathrm{d}r$, this becomes

$$\Gamma_{i,j} = \frac{2\pi \int_{r_{\min}}^{r_{\max}} r\sqrt{1+a^2}[(\nabla_S \Gamma)\sqrt{1+a^2}(r - r_{\min}) + c]\mathrm{d}r}{2\pi \int_{r_{\min}}^{r_{\max}} r\sqrt{1+a^2}\,\mathrm{d}r}, \tag{22}$$

where $r_{\max}$ is the radial location of the other endpoint. This equation is evaluated analytically and solved for c.

3.4. Volume fraction evolution

The governing equation for the volume fraction is written in axisymmetric, conservative form

$$\frac{\partial F}{\partial t} + \frac{1}{r}\frac{\partial}{\partial r}(ruF) + \frac{\partial}{\partial z}(vF) = F\left[\frac{1}{r}\frac{\partial}{\partial r}(ru) + \frac{\partial v}{\partial z}\right]. \tag{23}$$

The velocity divergence term is retained so that numerical error does not accumulate [60]. Following the methodology of [60], the equation is split into radial and vertical directions using an intermediate volume fraction, $\tilde{F}$,

$$\frac{\tilde{F}_{i,j} - F^n_{i,j}}{\Delta t} + \frac{RF^n_{i+1/2,j} - RF^n_{i-1/2,j}}{2\pi r_i \Delta r \Delta z \Delta t} = \tilde{F}_{i,j}\left(\frac{r_{i+1/2}u^{n+1}_{i+1/2,j} - r_{i-1/2}u^{n+1}_{i-1/2,j}}{r_i \Delta r}\right), \tag{24}$$

$$\frac{F^{n+1}_{i,j} - \tilde{F}_{i,j}}{\Delta t} + \frac{\tilde{Z}F_{i,j+1/2} - \tilde{Z}F_{i,j-1/2}}{2\pi r_i \Delta r \Delta z \Delta t} = \tilde{F}_{i,j}\left(\frac{v^{n+1}_{i,j+1/2} - v^{n+1}_{i,j-1/2}}{\Delta z}\right). \tag{25}$$

$RF_{i+1/2,j}$ is the volume flux of fluid 1 in the radial direction across the $(i+\frac{1}{2},j)$ face and $ZF_{i,j+1/2}$ is the volume flux of fluid 1 in the vertical direction across the $(i,j+\frac{1}{2})$ face. The volume of a grid cell is $2\pi r_i \Delta r \Delta z$. The fluxes are calculated in one direction and used to update the volume fraction to the intermediate level. Then, using the intermediate volume fraction, the fluxes are calculated in the other direction and used to update the intermediate volume fraction to the next time level. The direction computed first is switched at each time step.

The volume flux is the amount of fluid 1 that passes through the face during the time step. This flux equals the amount of fluid 1 in the domain of dependence of the face, at the beginning of the time step. This is illustrated in Fig. 4 for the case of flux across the $(i+\frac{1}{2},j)$ face with positive radial velocity, $u_{i+1/2,j}$. In general, the domain of dependence is approximated by the region bounded by the face of interest, the two adjacent perpendicular grid lines, and a line parallel to the face of interest that is a distance of $U\Delta t$ away from the face, where U is the velocity normal to the face. Recall that in axisymmetric coordinates this rectangular area represents a cylindrical volume. For the specific case shown in Fig. 4 these boundaries are $r = r_{i+1/2}$, $z = z_{j-1/2}$, $z = z_{j+1/2}$, and $r = r_{i+1/2} - u_{i+1/2,j}\Delta t$, respectively. Note that the sign of U determines which cell the domain of dependence is in and the sign of the flux. The flux is the intersection of the domain of dependence and the portion of the cell volume that contains fluid 1, as defined by a straight-line reconstruction of the interface.

3.5. Surface area evolution

As mentioned in Section 3.2 the accurate computation of the surface area is critical to the accurate computation of the surfactant concentration. Unfortunately, the area of the straight-line representation of the interface is a poor approximation of the actual interfacial area. The reason for this can be understood with reference to the example illustrated in Fig. 5. In this example, consider two adjacent grid cells with volume fractions $F_{i,j} = 0.9$ and $F_{i,j+1} = 0$. The interface reconstruction is shown in Fig. 5(a). If a constant vertical velocity, U, is applied, the region of fluid in cell (i,j) translates up by a distance $U\Delta t$ during a time step, as shown in Fig. 5(b). The interfacial area that is convected, A, is the area of that portion of the straight line that moves into cell $(i,j+1)$. However, when the interface is reconstructed from the new volume fraction distribution, as shown in Fig. 5(c), the interfacial area (according to the straight line approximation) is

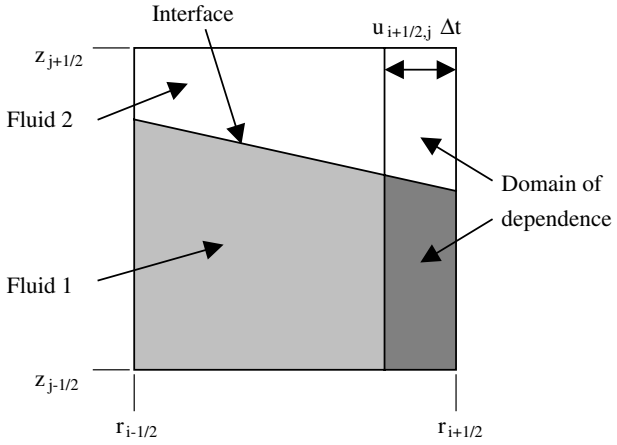

Fig. 4. Calculation of volume flux through $(i+\frac{1}{2},j)$ face. Fluid 1 lies below the line marked "interface" and fluid 2 lies above the line. The volume of fluid 1 fluxed through the face on the right, $RF_{i+1/2,j}$, is denoted by the darker gray area.

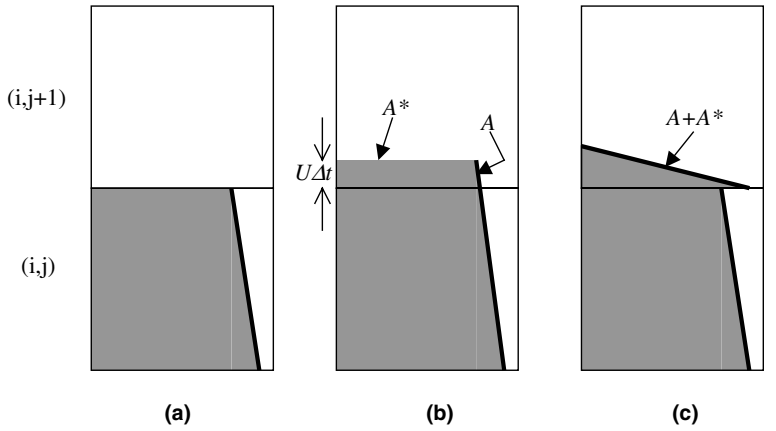

Fig. 5. Interfacial area evolution from linear interface reconstruction: (a) initial configuration, (b) translation, and (c) reconstruction.

approximately $A + A^*$ which is much larger than A because the cell boundary (which has area A^*) is interpreted as being part of the interface. Therefore, the interfacial area is tracked separately rather than using the area of the straight-line reconstruction.

Note that although this is a real problem, the example of Fig. 5 is somewhat exaggerated for clarity. In practice, a line segment that approximates the interface would not end far away from any other line segment, as shown in Fig. 5. Instead, another line segment would exist in the upper cell, although the endpoints of the two lines would not exactly coincide. This mismatch would lead to incorrect computation of the area because the cell boundary between the two endpoints would be interpreted as interfacial area.

Accuracy is also an important issue in cases where there is very little interface in a grid cell since the relative error in the area can become large. For example, both the interface area and the surfactant mass are small in such cells and therefore a small error in either the area or mass can lead to a large error in the surfactant concentration. This can then lead to artificially large gradients in surfactant concentration. We find, however, that such errors and the corresponding large gradients can be controlled by introducing a small amount of surfactant diffusion (e.g. $Pe_S \approx 1000$), which acts to smooth the gradients. At the same time, because of the fact that the surfactant mass in the affected cell is small, the overall effect of the diffusion is also small and thus the overall error remains small.

The interfacial area in a grid cell is governed by the following equation in conservative form:

$$\frac{\partial A}{\partial t} + \nabla \cdot (\underline{u}A) = -A(\underline{n} \cdot \nabla \underline{u} \cdot \underline{n}). \tag{26}$$

The area is updated in three steps. Two of these steps account for convection, one step in each direction, and are taken in tandem with the volume fraction. An additional step to account for stretching is taken in between the two convective steps:

$$\tilde{A}_{i,j} - A^n_{i,J} + RA^n_{i+1/2,j} - RA^n_{i-1/2,j} = 0, \tag{27}$$

$$\hat{A}_{i,j} = \tilde{A}_{i,j} - \Delta t \tilde{A}_{i,j}(\underline{n} \cdot \nabla \underline{u} \cdot \underline{n})^{n+1}_{i,j}, \tag{28}$$

$$A^{n+1}_{i,j} - \hat{A}_{i,J} + Z\hat{A}_{i,j+1/2} - Z\hat{A}_{i,j-1/2} = 0, \tag{29}$$

where $RA^n_{i+1/2,j}$ is the interfacial area flux in the radial direction across the $(i+\frac{1}{2},j)$ face, and $ZA^n_{i,j+1/2}$ is the interfacial area flux in the vertical direction across the $(i,j+\frac{1}{2})$ face. The stretching term in Eq. (28) is evaluated with second-order central differences. Convective fluxes of area are computed analogously to the volume fraction fluxes, and, as for the volume fraction, the direction computed first is switched at each time step. The fluxes in one direction are used to update the area to an intermediate value in all cells, $\tilde{A}$, at the same time the volume fraction is updated by convection in the same direction. The straight line interface reconstruction is then updated. Next, stretching is applied to update the area in all cells to $\hat{A}$. Finally, convective fluxes in the other direction complete the update of the area in all cells to the new time step, A^{n+1}. This is done in conjunction with the final update of the volume fraction by convection in the same direction.

Computation of the convective area flux is illustrated in Fig. 6 for the case of radial convection through the face $(i+\frac{1}{2},j)$. Computation of the fluxes across other faces is analogous. As for the volume fraction, the area flux is the area in the domain of dependence at the beginning of the time step. In Fig. 6 this domain is the region $u_{i+1/2,j}\Delta t$ wide. The area of the straight line in the domain of dependence is

$$A_{\mathrm{dod}} = 2\pi \int_{\mathrm{dod}} r\sqrt{1+a^2}\,\mathrm{d}r, \tag{30}$$

and the area of the straight line in the whole cell is

$$A_{\mathrm{sl}} = 2\pi \int_{\mathrm{cell}} r\sqrt{1+a^2}\,\mathrm{d}r. \tag{31}$$

Unlike in the volume fraction computation, A_{dod} is not an accurate representation of the area flux, as described above. However, the straight line does provide a good representation of which part of the cell the interface is in. Thus, we assume that the fraction of the actual area in the domain of dependence equals the fraction of the area of the straight line in the domain of dependence. Thus, the area flux is computed as the fraction of the area of the straight line in the domain of dependence, $A_{\mathrm{dod}}/A_{\mathrm{sl}}$, times the actual cell interfacial area, $A_{i,j}$,

$$\text{Area flux} = A_{i,j}\frac{A_{\mathrm{dod}}}{A_{\mathrm{sl}}}. \tag{32}$$

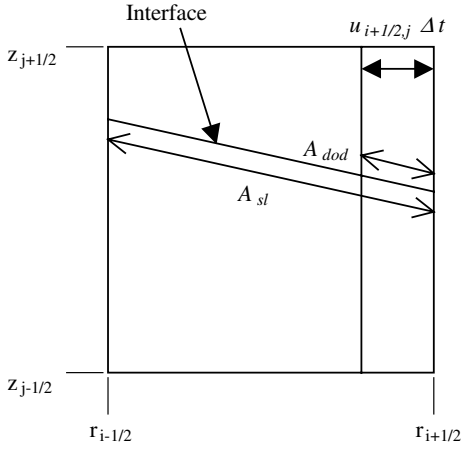

Fig. 6. Calculation of area flux through $(i+\frac{1}{2},j)$ face. The domain of dependence is the region of width $u_{i+1/2,j}\Delta t$ on the right side of the cell. The fraction of the cell area fluxed through the right face is the fraction of the straight-line area in the domain of dependence.

Current efforts are focused on developing a higher-order representation of the interface using parabolic segments. In this method the interface reconstruction will track the interfacial area correctly, making the reconstruction consistent with both the volume fraction and the area.

3.6. Surfactant evolution

Rather than solving Eq. (5) for the surfactant concentration, the surfactant mass is tracked. This approach has the advantage that surfactant mass conservation can be enforced directly. The concentration is also determined since it determines the surface tension and its gradient drives surface diffusion.

The evolution of the surfactant mass in a cell is governed by the following conservative convection–diffusion equation:

$$\frac{\partial M}{\partial t} + \nabla \cdot (\underline{u} M) = \frac{A}{Pe_S} \nabla_S^2 \Gamma. \tag{33}$$

At each time step, the mass equations are updated in three steps that correspond to convection and diffusion.

$$\tilde{M}_{i,j} - M^n_{i,J} + RM^n_{i+1/2,j} - RM^n_{i-1/2,j} = 0, \tag{34}$$

$$\hat{M}_{i,j} - \tilde{M}_{i,J} + Z\tilde{M}_{i,j+1/2} - Z\tilde{M}_{i,j-1/2} = 0, \tag{35}$$

$$M^{n+1}_{i,j} - \hat{M}_{i,j} = DR^{n+1}_{i+1/2,j} - DR^{n+1}_{i-1/2,j} + DZ^{n+1}_{i,j+1/2} - DZ^{n+1}_{i,j-1/2}. \tag{36}$$

First, the mass is updated in every cell to an intermediate level, $\tilde{M}$, by convection in one direction, along the convection of volume fraction and interfacial area in the same direction. After this the interface approximation is reconstructed, the area is stretched, the average concentration is updated as $\Gamma = M/A$, Eq. (6), and the concentration approximation is reconstructed. Next, the mass is updated in every cell by convection in the other direction to $\hat{M}$, along with convection of volume fraction and interfacial area. The direction in which F, A and M are convected first is switched at every time step to avoid skew. Then, once again, the interface approximation is reconstructed, the average concentration is updated using Eq. (6), and the concentration approximation is reconstructed. Finally, the mass is updated in every cell to the next time level, M^{n+1}, by diffusion in both directions simultaneously.

The mass fluxed by convection through a cell face during a time step equals the mass in the domain of dependence at the beginning of the step, as for volume of fluid and interfacial area. Its computation is analogous to the area flux computation. A first approximation to the flux is the integral of the concentration over the straight line in the domain of dependence

$$M_{\mathrm{dod}} = 2\pi \int_{\mathrm{dod}} r\sqrt{1+a^2}[(\nabla_S \Gamma)\sqrt{1+a^2}(r - r_{\min}) + c]\mathrm{d}r. \tag{37}$$

In Eq. (37) it is crucial to use the linear reconstruction of the concentration, instead of simply its average value, to avoid excessive numerical diffusion. As for the area, this does not accurately represent the flux since M_{dod} is obtained using the straight line. However, $M_{\mathrm{dod}}/A_{\mathrm{dod}}$ gives a consistent value for the average concentration on the portion of the interface that is convected. This is multiplied by the area flux to obtain a mass flux that is consistent with the area flux

$$\text{Mass flux} = \left(\frac{M_{\mathrm{dod}}}{A_{\mathrm{dod}}}\right)\left(A_{i,j}\frac{A_{\mathrm{dod}}}{A_{\mathrm{sl}}}\right). \tag{38}$$

Next, the mass is updated to the new time step by diffusion in a single implicit step. Diffusion of surfactant across a cell face occurs only when there is an interface in both cells adjacent to the face. From Fick's law, the radial flux across the face $(i+\frac{1}{2},j)$, for example, is

$$DR^{n+1}_{i+1/2,j} = \frac{\Delta t}{Pe_S} 2\pi r_{i+1/2} \left(\frac{\partial \Gamma}{\partial s}\right)^{n+1}_{i+1/2,j}. \tag{39}$$

This can also be obtained from Eq. (11) as follows. For axisymmetric coordinates $\underline{n} \times \hat{n}_V = \pm\hat{\theta}$ (the azimuthal direction) is the tangent to curve C, $\underline{n} \times \hat{n}_V \times \underline{n}$ is the tangent to the interface in the $r-z$ plane pointing out of the grid cell, and so $(\underline{n} \times \hat{n}_V \times \underline{n}) \cdot \nabla_S \Gamma$ becomes the scalar derivative of Γ in this tangent direction. The length of the curve C is $2\pi r$. Eq. (39) can be approximated, as illustrated in Fig. 7, by

$$DR^{n+1}_{i+1/2,j} = \frac{\Delta t}{Pe_S} 2\pi r_{i+1/2} \left(\frac{\Gamma^{n+1}_{i+1,j} - \Gamma^{n+1}_{i,j}}{L_{i+1/2,j}}\right), \tag{40}$$

where the surface gradient is approximated as the difference in the average concentration between the two cells, divided by L, the distance between the midpoints of the straight-line interface reconstructions in the two cells adjacent to the face. In Fig. 7 the difference between the slopes of the two segments is exaggerated for clarity. Although the slope is not constrained to vary slowly from one cell to the next, in practice it generally does vary slowly. If $DR_{i+1/2,j}$ is positive surfactant is fluxed from cell $(i+1,j)$ to cell (i,j), or from higher to lower concentration. The flux across a face is set to zero if there is no interface in either of the adjacent cells. Note that Eq. (36) is implicit, since the concentration in the flux is evaluated at the new time step. In practice this is written as an equation for concentration by dividing by the area

$$\Gamma^{n+1}_{i,j} = \hat{\Gamma}_{i,j} + (DR^{n+1}_{i+1/2,j} - DR^{n+1}_{i-1/2,j} + DZ^{n+1}_{i,j+1/2} - DZ^{n+1}_{i,j-1/2})/A^{n+1}_{i,j}. \tag{41}$$

Since the fluxes depend on $\Gamma^{n+1}_{i,j}$ this coupled system is solved iteratively for $\Gamma^{n+1}_{i,j}$ in all cells using the point Gauss–Seidel method. The surfactant mass is then updated as $M = \Gamma A$.

3.7. Surface tension force

Once the surfactant concentration distribution is known the average surface tension in each grid cell can be computed from the equation of state, Eq. (15) or (14). The surface tension force, Eq. (3), can be written as

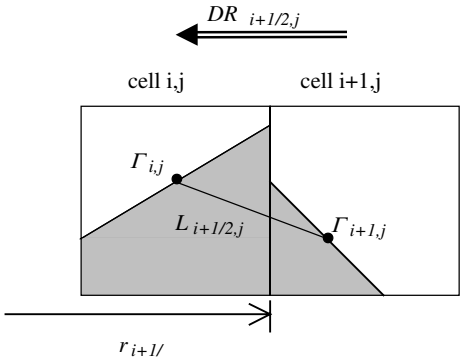

Fig. 7. Schematic of surfactant diffusion flux computation.

$$\underline{F_S} = \sigma\kappa\nabla F + \frac{\partial\sigma}{\partial s}|\nabla F|\underline{s}. \tag{42}$$

In the staggered grid arrangement the radial component of this force is computed at $(i+\frac{1}{2}, j)$ cell faces and the vertical component at $(i, j+\frac{1}{2})$ cell faces. First, the curvature is computed in each grid cell center from a smoothed volume fraction using standard methods [35]. Next, the curvature is evaluated at each face as the average of the curvature in the two adjacent cells, e.g.

$$\kappa_{i+1/2,j} = \frac{\kappa_{i,j} + \kappa_{i+1,j}}{2}. \tag{43}$$

The surface tension at cells faces is also computed as the average of the surface tension in the two adjacent cells, if both cells contain an interface segment. If only one of the adjacent cells contains an interface segment the surface tension in that cell is used as the surface tension at the face. If there is not an interface segment in either adjacent cell the surface tension at the face is set to zero and there is no normal force.

The surface gradient of the surface tension is also non-zero only at faces for which both adjacent grid cells contain an interface segment. For such faces the gradient is computed exactly as the surface gradient of concentration is computed in evaluating surface diffusion, as illustrated in Fig. 7. First the distance between the interface midpoints is computed. The gradient is then the difference in the surface tension between the two cells divided by this distance, L. Since the cell face is not necessarily halfway between the interface midpoints the method is not strictly second order accurate in space. The magnitude of the volume fraction gradient at each face is computed using straightforward second-order finite difference approximations. Finally, the radial and vertical components of the surface stress, FR and FZ, respectively, are

$$FR_{i+1/2,j} = (\sigma\kappa)_{i+1/2,j}\left(\frac{F_{i+1,j} - F_{i,j}}{\Delta r}\right) + \left(\frac{\sigma_{i+1,j} - \sigma_{i,j}}{L_{i+1/2,j}}\right)|\nabla F|_{i+1/2,j}, \tag{44}$$

$$FZ_{i,j+1/2} = (\sigma\kappa)_{i,j+1/2}\left(\frac{F_{i,j+1} - F_{i,j}}{\Delta z}\right) + \left(\frac{\sigma_{i,j+1} - \sigma_{i,j}}{L_{i,j+1/2}}\right)|\nabla F|_{i,j+1/2}. \tag{45}$$

Another method of evaluating the surface stress is to consider the surface tension force, $\underline{F_{AB}}$, on a straight line segment that approximates the interface in a grid cell. The line segment with endpoints A and B, and

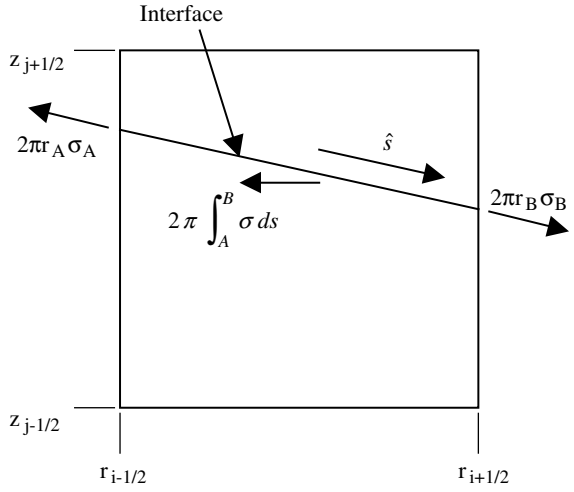

Fig. 8. Definitions of interface geometry and surface force in (i,j) cell.

the surface tension force are illustrated in Fig. 8. A unit tangent vector in the r–z plane, $\hat{s}$, is defined pointing from A to B. In the axisymmetric geometry, the surface tension force along an interface segment (not necessarily straight) is

$$\underline{F_{AB}} = 2\pi r_B \sigma_B \hat{s_B} - 2\pi r_A \sigma_A \hat{s_A} - 2\pi \hat{r} \int_A^B \sigma \, \mathrm{d}s, \tag{46}$$

where s is the spatial coordinate directed from A to B along the interface. This equation is derived in Appendix B; to our knowledge this formula has not previously appeared in the literature for variable surface tension. From this force the surface stress applied in the momentum equation is obtained by dividing by the cell volume. This form of the surface stress is used to obtain exact values of the surface force that are used to compare with discretizations of Eq. (42). These results are shown in the next section. The numerical implementation of Eq. (46) will be explored in future work.

4. Validation

A number of test cases were performed to validate the algorithms. Testing of the flow solver and volume fraction advection routines have been reported elsewhere [35,59] and will not be discussed here. In the first set of tests the flow solver is turned off and the velocity field is prescribed to isolate the new surfactant kinematics algorithms from the flow solver. Convection of the interfacial area and the surfactant are tested in several configurations without surfactant diffusion. Next, surfactant diffusion on a fixed interface is tested without convection. The surfactant distribution is then specified to test the implementation of the surface tension force. Finally, the flow solver is turned on and tests are performed involving solution of all the equations coupled together in some simple flows. Throughout this section if an exact solution is known an L_1 error will be defined as

$$L_1 \text{ Error} = \frac{\sum_{\text{cells}} |\chi_{i,j} - \chi_{i,j}^{\text{exact}}|}{\text{number of cells}}, \tag{47}$$

where χ can represent any dependent variable.

In several test cases we find a non-integer order of accuracy and in some tests the error appears to saturate as the grid is refined. There are several effects that may cause this. First, more than one type of error may be important. For example, in the convection tests there are errors due to both convection and stretching, and it is not easy to separate the two. Second, although the interface is not explicitly discretized there is a discretization implied in the way the interface cuts through the grid. This discretization is non-uniform in all but the simplest test cases. When the grid is refined this implicit interface discretization is not refined uniformly. Thus, the error may not decrease in a predictable way. Finally, there are several iterative procedures that may not be fully converged, particularly when the grid is fine.

4.1. Surfactant convection tests

4.1.1. 1D convection tests

Four 1D tests in the radial and vertical directions were performed to check the algorithm that convects the interface and the surfactant. In each direction, motion tangential and normal to the interface were tested separately. In each case a velocity field was imposed and the evolution of the volume fraction, interface area, surfactant mass, and surfactant concentration was computed. The surfactant concentration was initially uniform and should remain so.

In the first three tests the interface was represented exactly by the staight line reconstruction, so the results were exact within round-off error. These tests were: (i) radial convection of surfactant along a fixed horizontal interface, (ii) vertical convection of surfactant along a fixed vertical interface, and (iii) vertical convection of surfactant with a vertically translating horizontal interface.

In the last 1D test the interface was initialized as a cylinder, with radius $r = R$, with a uniform surfactant concentration. A line source on the symmetry axis and a divergence-free, radially-directed velocity, $\underline{u} = (1/r)\hat{r}$, were imposed. Thus, the volume fraction, interfacial area, surfactant mass, and surfactant concentration were convected outward with the interface. In this case the error is non-zero because there is stretching of the interface. The stretching term is evaluated at cell centers instead of at the interface. This does not affect the volume fraction, which is still exact within round-off error. Additionally, the surfactant mass is exact within round-off error since mass conservation is imposed exactly. The effect of grid resolution on the error in the interfacial area and the surfactant concentration is shown in Fig. 9. The slope of the least-squares fit is 4.4 for the area error and 3.4 for the surfactant concentration error.

The difference in accuracy between the area error and surfactant concentration error can be explained as follows. In an interfacial grid cell with a concentration of one, the exact area and mass are both $2\pi R\Delta z$. Considering the $O(\Delta z^{4.4})$ error in the area due to stretching, the concentration becomes

$$\Gamma = \frac{M}{A} = \frac{2\pi R\Delta z}{2\pi R\Delta z + O(\Delta z^{4.4})} = \frac{1}{1 + O(\Delta z^{3.4})} = 1 + O(\Delta z^{3.4}). \tag{48}$$

In more general situations where the interface shape is arbitrary, if the concentration is O(1) the area and mass are still both $O(\Delta z)$ (assuming the grid spacing is the same in the radial and vertical directions, which it always is in practice). If the area error is $O(\Delta z^n)$ and the mass error is $O(\Delta z^m)$, then the concentration becomes

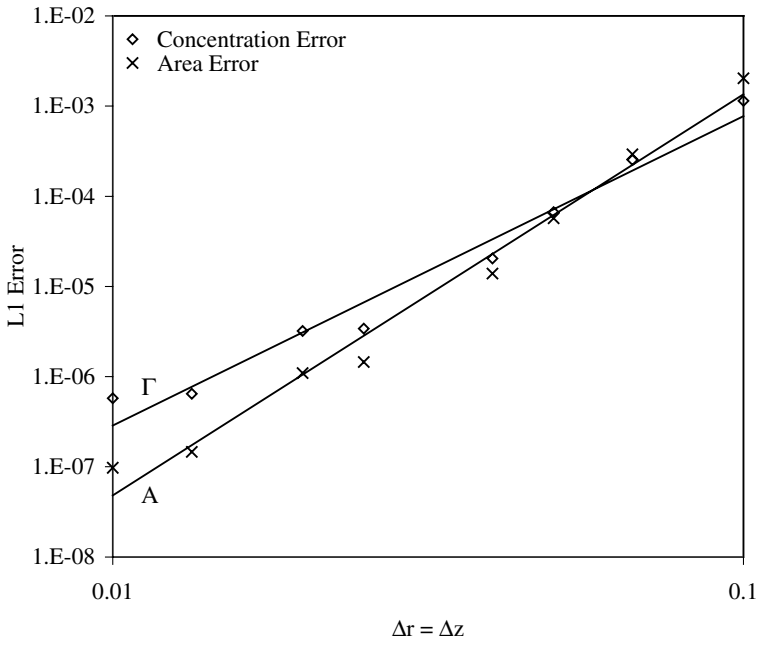

Fig. 9. Effect of grid resolution on error in the interfacial area and surfactant concentration on the surface of an expanding cylinder. Domain: 1×2, initial cylinder volume: $\frac{1}{4}$, initial concentration: 1, Courant number: 0.1, time elapsed: $\frac{1}{4}$. Symbols are computed errors and solid lines are least-squares fits.

$$\Gamma = \frac{M}{A} = \frac{O(\Delta z) + O(\Delta z^m)}{O(\Delta z) + O(\Delta z^n)} = \frac{O(1) + O(\Delta z^{m-1})}{O(1) + O(\Delta z^{n-1})} = O(1) + O(\Delta z^{m-1}) + O(\Delta z^{n-1}). \tag{49}$$

Thus, the concentration is one order less accurate than the least accurate of the mass and area.

4.1.2. Axisymmetric convection test

Next, a test was performed involving convection in the radial and vertical directions simultaneously. A sphere of volume $\frac{1}{4}$ was initialized in a 1×2 domain. Since the interface was spherical, the straight-line approximation was not exact. A divergence-free velocity,

$$\underline{u} = \frac{r\hat{r} + (z - z_0)\hat{z}}{\left[r^2 + (z - z_0)^2\right]^{3/2}}, \tag{50}$$

was imposed, where $z_0 = 1$ is the fixed vertical location of the sphere center. This velocity field is normal to the interface and causes the sphere to expand. Thus, there was error due to stretching. Additionally, the surfactant concentration was initially non-uniform, with an exact solution

$$\Gamma(\phi, t) = \left(\frac{1 + \cos\phi}{2}\right)\left(\frac{1}{16\pi t + 1}\right)^{1/3}, \tag{51}$$

where ϕ is the angular coordinate measured from the pole of the sphere. The shape of the concentration profile is constant, but the magnitude decreases as the surface area of the sphere increases. The results are reported after an elapsed time of $t = \frac{1}{4}$. At this time the sphere surface is nearing the domain boundaries.

The effect of grid resolution on the error in the volume fraction, interfacial area, surfactant mass and surfactant area is shown in Fig. 10. The slope of the least-squares fit is 1.3 for the volume fraction error, 2.3 for the area error, 3.6 for the surfactant mass error, and 3.3 for the surfactant concentration error. The concentration error is nonlinear due to round off error in the high resolution cases. This comes about be-

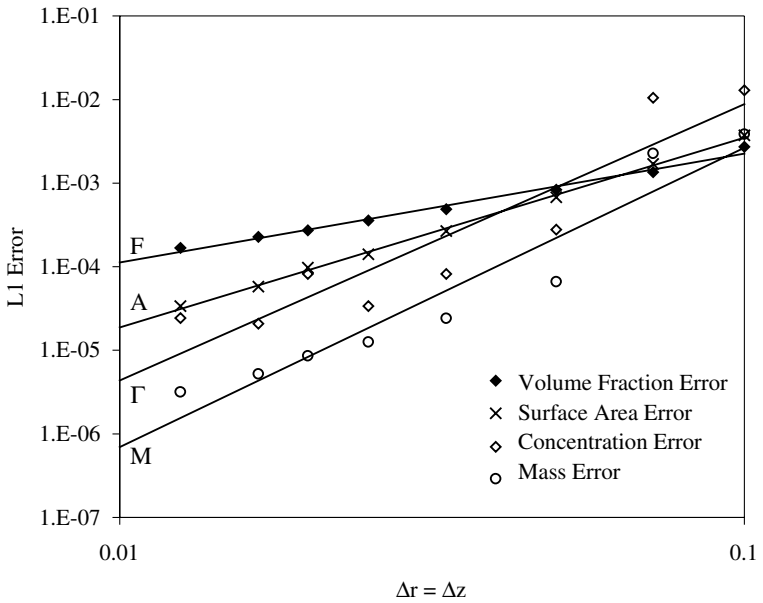

Fig. 10. Effect of grid resolution on error for an expanding sphere. Domain: 1×2, initial sphere volume: $\frac{1}{4}$, Courant number: 0.1, time elapsed: $\frac{1}{4}$. Symbols are computed errors and solid lines are least-squares fits.

cause the concentration is mass divided by area, which both become small as the grid is refined. Division of one small number into another is sensitive to round-off errors. Inclusion of a small amount of diffusion in the computations aleviates this sensitivity by smoothing away the error. The effect of diffusion is illustrated in the next section.

4.2. Surfactant diffusion tests

In this set of test cases the interface is stationary, and the velocity is fixed at zero. The surfactant is initialized nonuniformly on the interface, and it diffuses along the interface to become uniform. Three configurations are considered. First, the interface is a flat layer and the diffusion is purely radial. Second, the interface is a cylinder and the diffusion is purely vertical. Finally, the interface is a sphere and both radial and vertical components of diffusion are present. The exact solutions are

$$\Gamma(r,t) = \frac{1}{2} + \frac{1}{2}\exp\left(\frac{-\zeta^2 t}{Pe_S}\right) J_0(\zeta r) \text{ on a flat layer,} \tag{52}$$

$$\Gamma(z,t) = \frac{1}{2} + \frac{1}{2}\exp\left(\frac{-\zeta^2 t}{Pe_S}\right) \cos(\zeta z) \text{ on a cylinder,} \tag{53}$$

$$\Gamma(\phi,t) = \frac{1}{2} + \frac{1}{2}\exp\left(\frac{-2t}{Pe_S R^2}\right) \cos\phi \text{ on a sphere,} \tag{54}$$

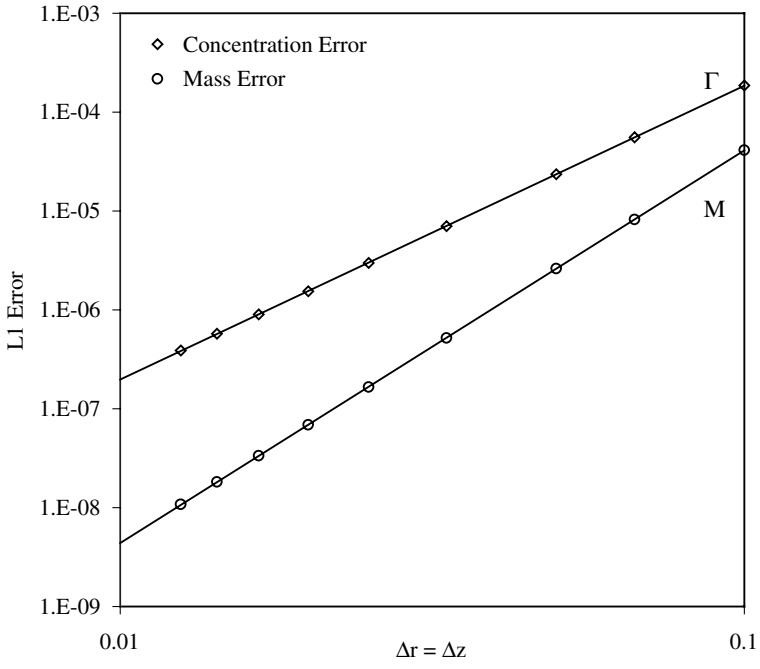

Fig. 11. Effect of grid resolution on surfactant mass and surfactant concentration errors during radial diffusion on a flat interface. Domain: 1×1, layer volume: 1, von Neumann number: 0.5, time elapsed: 0.0625, $Pe_S = 1$, 5 iterations in diffusive evolution. Symbols are computed errors and solid lines are least-squares fits.

where ζ is an eigenvalue determined by the boundary conditions, and R is the sphere radius. In each geometry the surfactant mass and concentration are initialized with the exact solution and then allowed to evolve.

For diffusion on a flat layer of unit volume the domain was 1×1 units. The surfactant mass and surfactant concentration errors are shown in Fig. 11 as functions of grid resolution. The slope of the least-squares fit is 4.0 for the mass error and 3.0 for the concentration error.

For diffusion on a cylinder of volume $\frac{1}{4}$ the domain was 1×2 units. The surfactant mass and surfactant concentration errors are shown in Fig. 12 as functions of grid resolution. The slope of the least-squares fit is 3.0 for the mass error and 2.0 for the concentration error.

Similar results are shown in Fig. 13 for diffusion on a spherical interface. The domain was 1×2 units and the sphere volume was $\frac{1}{4}$. The surfactant mass and concentration errors are plotted as a function of the grid resolution. The slope of the least squares fit is 3.9 for the mass error and 2.7 for the concentration error. The error is not a smooth function of the number of cells in this case. For the layer and the cylinder, the interface cut through the grid such that the distance between interface midpoints was the same in all cells and this distance decreased linearly with the grid spacing. For the sphere the interface cuts through the grid non-uniformly. Although the distance between interface midpoints decreases on average as the grid spacing is decreased, locally it may decrease in some places and increase in others. However, the overall trend shows that the error decreases as the grid is refined.

Diffusion on the surface of a sphere was also used to determine the effect of the number of iterations in the solution for the diffusive evolution. Fig. 14 shows the concentration and mass errors as a function of the number of iterations. The error drops rapidly in the first two iterations and then does not change.

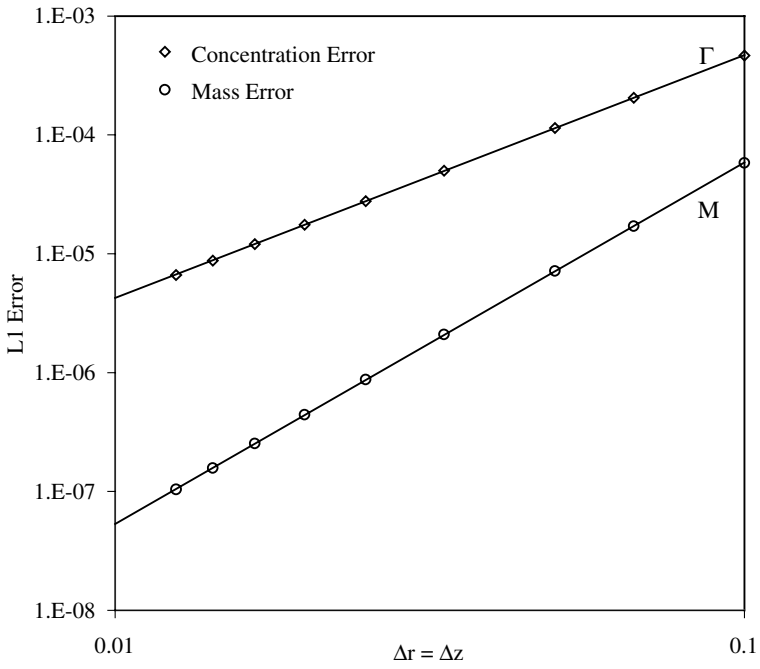

Fig. 12. Effect of grid resolution on surfactant mass and surfactant concentration errors during vertical diffusion on a cylindrical interface. Domain: 1×2, cylinder volume: $\frac{1}{4}$, von Neumann number: 0.5, time elapsed: 0.025, $Pe_S = 1$, 5 iterations in diffusive evolution. Symbols are computed errors and solid lines are least-squares fits.

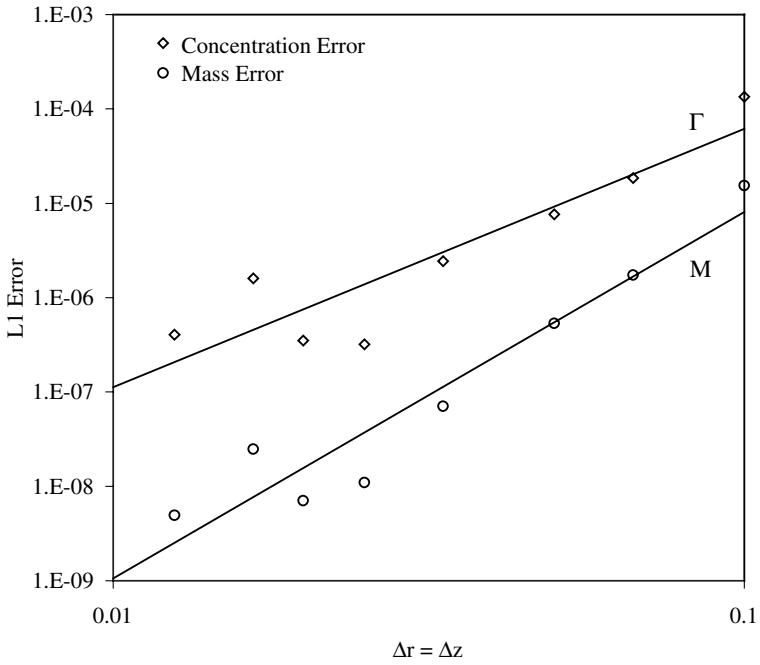

Fig. 13. Effect of grid resolution on surfactant mass and concentration errors during diffusion on a spherical interface. Domain: 1×2, sphere volume: $\frac{1}{4}$, von Neumann number: 0.1, time elapsed: 0.25, $Pe_S = 1$, 5 iterations in diffusive evolution. Symbols are computed errors and solid lines are least-squares fits.

4.3. Surface force validation

This static test was designed to check the computation of the surface tension force, independently of all other algorithms. The flow solver was not used. The volume fraction, surface area, surfactant mass and surfactant concentration were fixed using the exact solution.

The domain was 1×2 units. The volume fraction and surface area were initialized for a sphere for volume $\frac{1}{4}$. The surfactant mass and concentration were initialized for

$$\Gamma(\phi) = \left(\frac{1 + \cos\phi}{2}\right). \tag{55}$$

The linear equation of state was used. The exact force was computed using Eq. (46). The error reported is the average of the L_1 errors of the radial and vertical components of the force. The effect of grid resolution on the error is shown in Fig. 15. The slope of the least-squares fit is 1.7.

4.4. Static drop

In this and the subsequent test cases the flow equations were solved, as well the equations governing interface and surfactant motion. In this test a spherical drop of radius R is initialized with zero velocity, uniformly distributed surfactant, zero pressure outside the drop, and pressure $p_{\text{theory}} = 2/(R\,Re\,Ca)$ inside the drop to balance surface tension. Such a drop should ideally remain static, but numerical mismatch between the pressure and surface tension forces leads to motion. The interface position adjusts to balance pressure and surface tension.

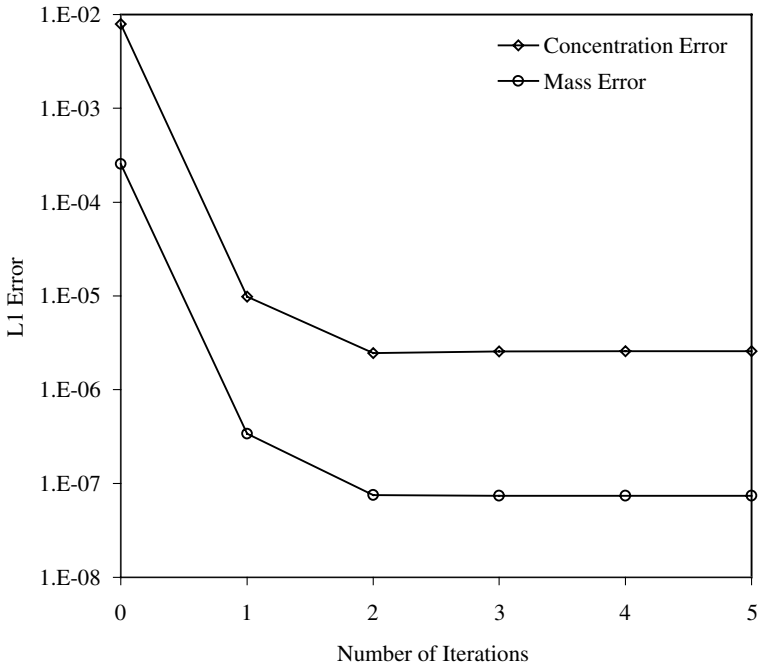

Fig. 14. Effect of the number of iterations in the diffusive evolution on surfactant mass and concentration errors during diffusion on a spherical interface. Domain: 1×2, sphere volume: $\frac{1}{4}$, von Neumann number: 0.1, time elapsed: 0.25, $Pe_S = 1$, 30×60.

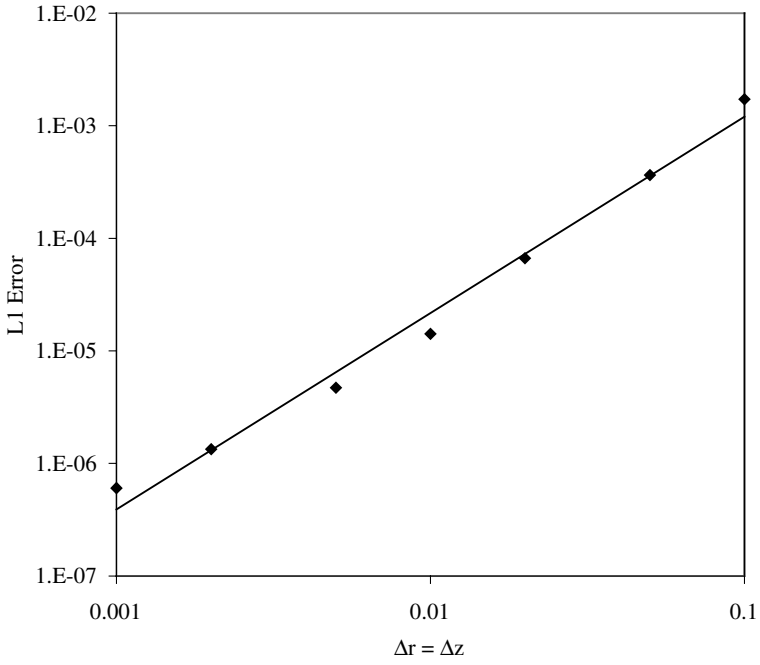

Fig. 15. Effect of grid resolution on error in surface tension force. Domain: 1×2, sphere volume: $\frac{1}{4}$, $\beta = 0.2$. Symbols are computed error and solid line is least-squares fit.

This test was configured to match similar 3D, surfactant-free tests of Kothe et al. [61] with $Ca = Re = 1$. The sphere radius was 4. The domain was 8×16. The solution was advanced one time step and then the pressure field was compared to the theoretical pressure field used in the initialization. Since the solution is only advanced one step the values of the time step, the viscosity ratio and the surface Peclet number do not effect the results. The presence of surfactant also has no effect on the results since the surfactant is uniform.

A density ratio of $\alpha = 0.5$ was chosen to allow comparison to the results of [61]. They quantified the pressure change using an L_2 error norm

$$L_2 \text{ error} = \sqrt{\sum (2\pi r_i \Delta r \Delta z)^2 \left(\frac{p_{i,j} - p_{\text{theory}}}{p_{\text{theory}}} \right)^2}. \tag{56}$$

This error is presented in Fig. 16 as a function of grid resolution. Kothe et al. [61] only presented two data points for this density ratio at fairly flow resolution, but the results appear to be consistent. A least-squares curve fit of the present results has a slope of 1.2.

4.5. Marangoni convection

The previous test is modified by applying a nonuniform initial surfactant concentration and allowing the solution to evolve in time. Since the concentration is nonuniform the surface tension is nonuniform and there is a Marangoni force that causes motion. This motion redistributes the surfactant, which eventually becomes uniform.

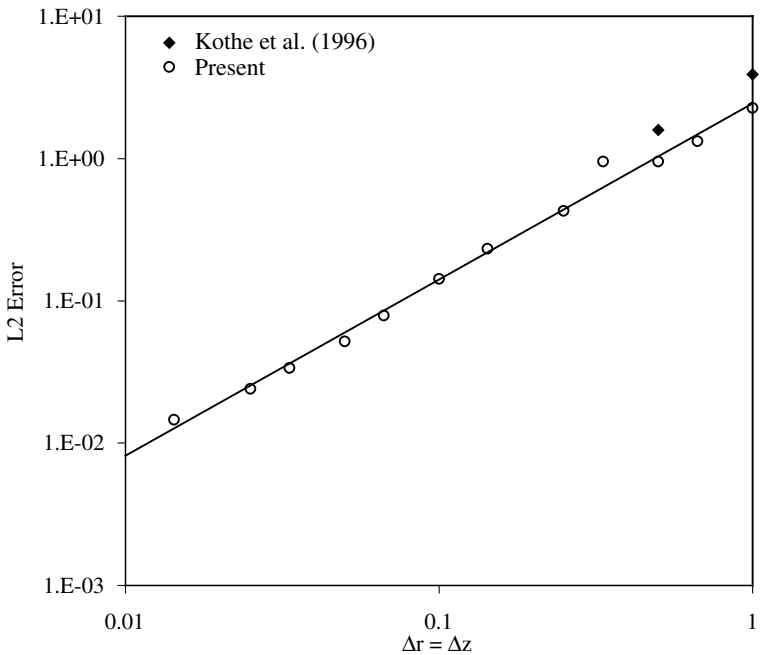

Fig. 16. Effect of grid resolution on pressure error in static drop. Domain: 8×16, sphere radius: 4, $\alpha = \frac{1}{2}$. Closed symbols are error computed by [61], open symbols are present error results, solid line is least-squares fit to present results.

A static sphere with volume $\frac{1}{4}$ is initialized in a 1×2 domain. The pressure is initally zero outside the drop and $2/(R\,Re\,Ca)$ inside the drop to balance the average surface tension force, where R is the sphere radius. The surfactant mass and concentration are initialized by Eq. (55). The density and viscosity of the inner and outer fluids are matched and $Re = Ca = 1$. Both the linear and nonlinear equation of state are used. The effect of grid resolution and variations in the Peclet number were considered.

The evolution of the surfactant distribution on the sphere surface is shown in Fig. 17 for a typical case. As the simulation progresses the concentration becomes more uniform due to both diffusion and Marangoni convection. For the cases considered, the drop deforms very little. The total surface area typically changes by less than 2%.

The effect of the Peclet number is illustrated in Fig. 18, where the surfactant concentration as a function of position on the interface is shown at $t = 1$. For smaller Peclet number diffusion dominates, so the concentration becomes uniform quickly and the Marangoni force is relatively unimportant. When the Peclet number is large, the concentration is not as smooth, since there is little diffusion or numerical smoothing.

The concentration profile is shown in Fig. 19 for various grid resolutions at $t = 1$. A Peclet number of 1000 was chosen to minimize smoothing and provide a more stringent test. It is clear that the non-physical oscillations in the solution are smaller when the grid resolution is higher.

Finally, the difference in the evolution due to the equation of state is illustrated for two cases in Figs. 20 and 21. In both cases the strength of the Marangoni force is matched between the linear and nonlinear EOS cases by setting $\beta = Ex$. The coverage, and hence β, is greater in Fig. 21 than in Fig. 20. The linear equation of state approximates the nonlinear equation of state in the limit of small surfactant coverage, so it is expected that the results between the two equations of state differ more in Fig. 21 where the coverage is higher.

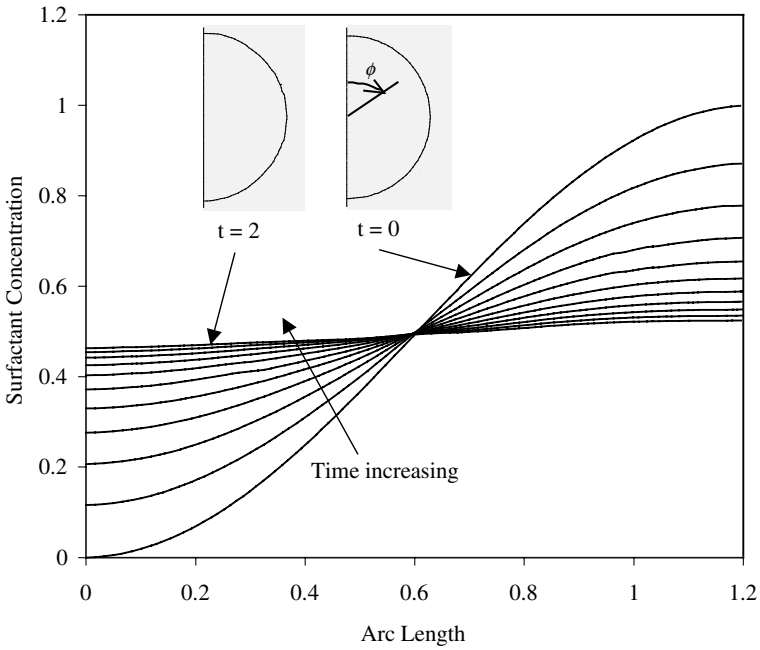

Fig. 17. Evolution of surfactant concentration on the surface of a deformable sphere. Domain: 1×2, 60×120 grid cells, $\alpha = \lambda = Re = Ca = 1$, $Pe_S = 10$, linear equation of state with $\beta = 0.1$. The insets show surfactant concentration contours, ranging from zero (white) to one (black), at the initial ($t = 0$) and final ($t = 2$) times.

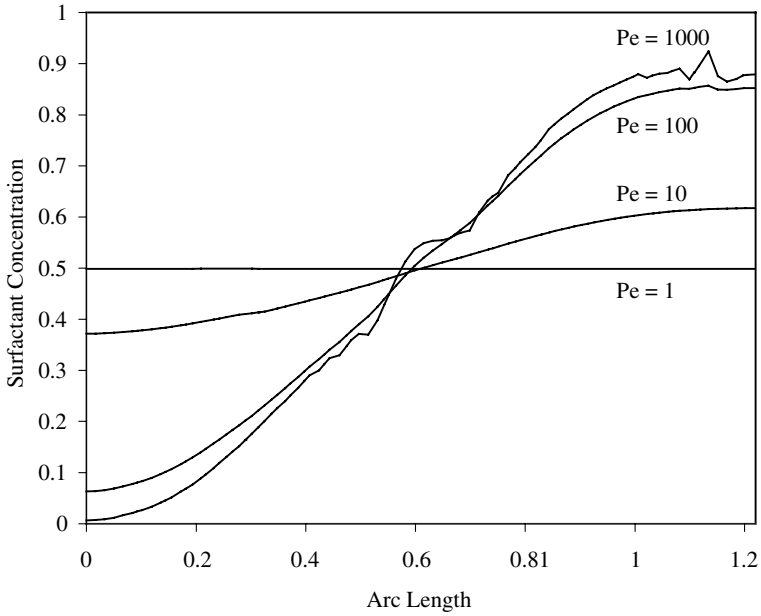

Fig. 18. Effect of Peclet number on surfactant concentration profile. Domain: 1×2, 60×120 grid cells, $\alpha = \lambda = Re = Ca = 1$, $t = 1$, linear equation of state with $\beta = 0.1$.

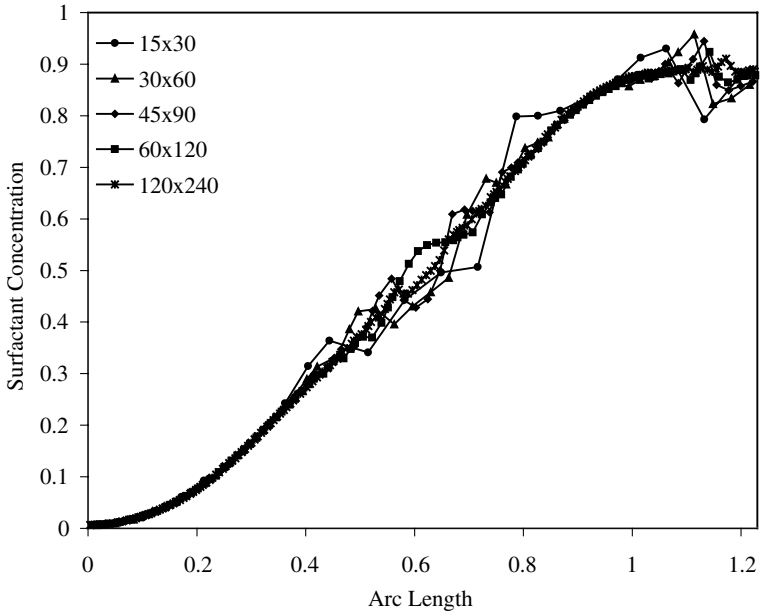

Fig. 19. Effect of grid resolution on surfactant concentration profile. Domain: 1×2, $\alpha = \lambda = Re = Ca = 1$, $Pe_S = 1000$, $t = 1$, linear equation of state with $\beta = 0.1$.

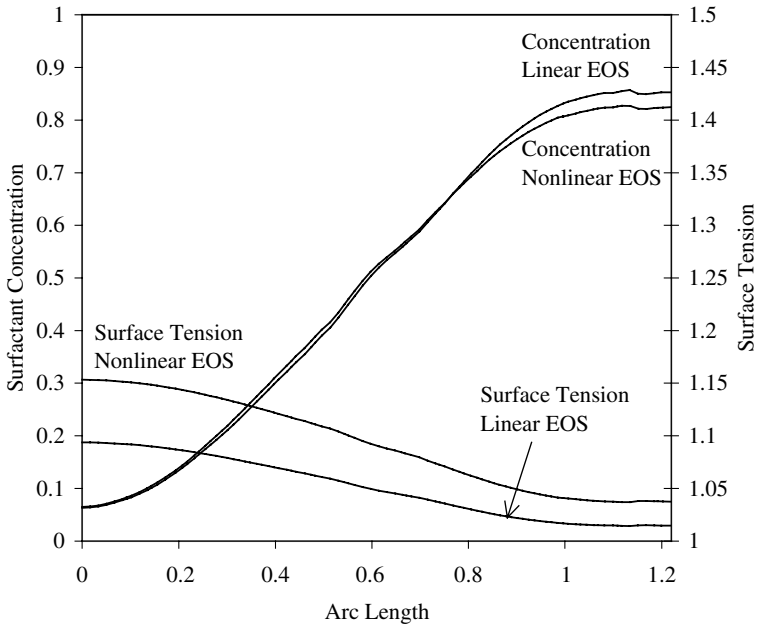

Fig. 20. Surfactant concentration and surface tension profiles. Domain: 1×2, $\alpha = \lambda = Re = Ca = 1$, $Pe_S = 100$, $t = 1$. Nonlinear equation of state uses $E = 0.2$ and $x = 0.5$, and linear equation of state uses $\beta = Ex = 0.1$.

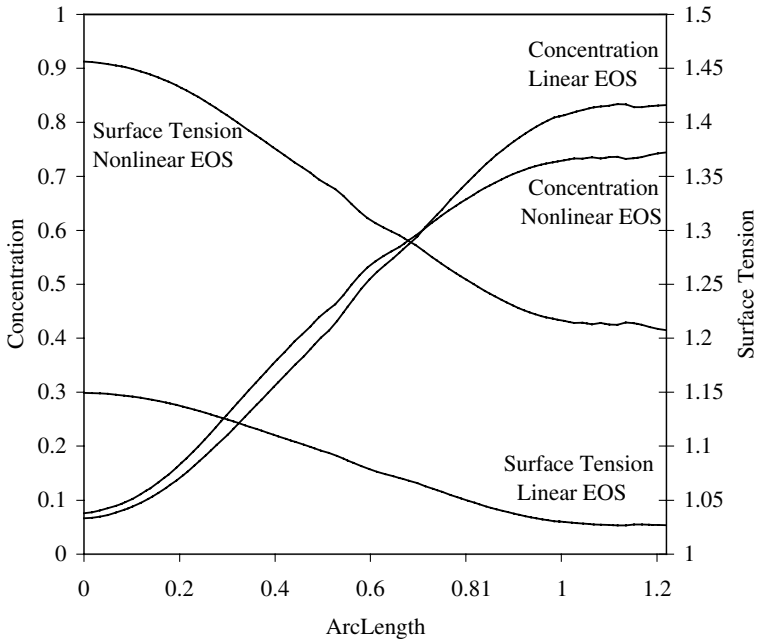

Fig. 21. Surfactant concentration and surface tension profiles. Domain: 1×2, $\alpha = \lambda = Re = Ca = 1$, $Pe_S = 100$, $t = 1$. Nonlinear equation of state uses $E = 0.2$ and $x = 0.8$, and linear equation of state uses $\beta = Ex = 0.16$.

4.6. Drop extension

Next, we consider the evolution of a drop subjected to extension for three cases. One case is surfactant-free, one case includes surfactant with a linear equation of state, and one case includes surfactant with a nonlinear equation of state that matches the linear equation in the dilute limit (coverage $x \to 0$). The viscosity and density ratios are $\lambda = 1$ and $\alpha = 1$, respectively. In each case a sphere of unit radius is initialized with an applied velocity field $\underline{u} = (-r, 2z)$. The Reynolds and Capillary numbers are $Re = 1$ and $Ca = 0.05$. This velocity field is then maintained on the boundaries and the drop is allowed to evolve. For the cases with surfactant, the concentration is initially uniform and is dilute with coverage $x = 0.1$ in the nonlinear case (elasticity $E = 0.2$) while in the linear case $\beta = 0.02$. Later we will examine the effect of the coverage.

The evolution of the drop shape is shown in Fig. 22 for the three cases (the $F = 0.5$ contour is plotted). The drop shapes show that the case without surfactant is stretched the least and the case with nonlinear surfactant is stretched the most. Fig. 23 shows the evolution of the surfactant concentration grey-scale contours (right side of drop) for the case with nonlinear surfactant. The left side is the drop interface $F = 0.5$. The case with linear surfactant looks qualitatively very similar. This figure shows that as the drop is stretched the outer flow sweeps surfactant to the tips of the drop. Thus, the surface tension is lower at the tips and higher in the center. Because of this the drop tends to thin more in the center and has less resistance to stretching at the tips resulting in increased stretching for the cases with surfactant. Note that the (insoluble) surfactant remains bound to the drop interface.

To compare the two cases with surfactant, in Fig. 24 the surfactant concentration (top) and surface tension (bottom) are plotted as functions of arclength (arclength increases towards the drop tip) at the final time shown in Fig. 22. Observe that the surfactant concentration is higher at the drop tip for the linear

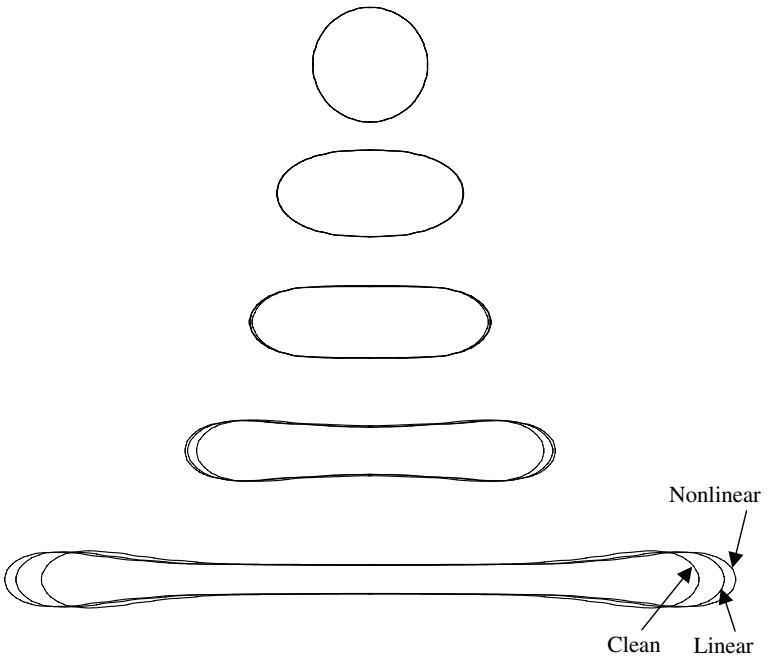

Fig. 22. Evolution of a drop subjected to extension. Domain: 2×10, 30×150 grid cells, time increment between images = 0.5, $Re = 1$, $Ca = 0.05$, $Pe_S = 100$, $\alpha = \lambda = 1$, $\beta = 0.02$ for surfactant with linear equation of state, $E = 0.2$, and $x = 0.1$ for surfactant with nonlinear equation of state.

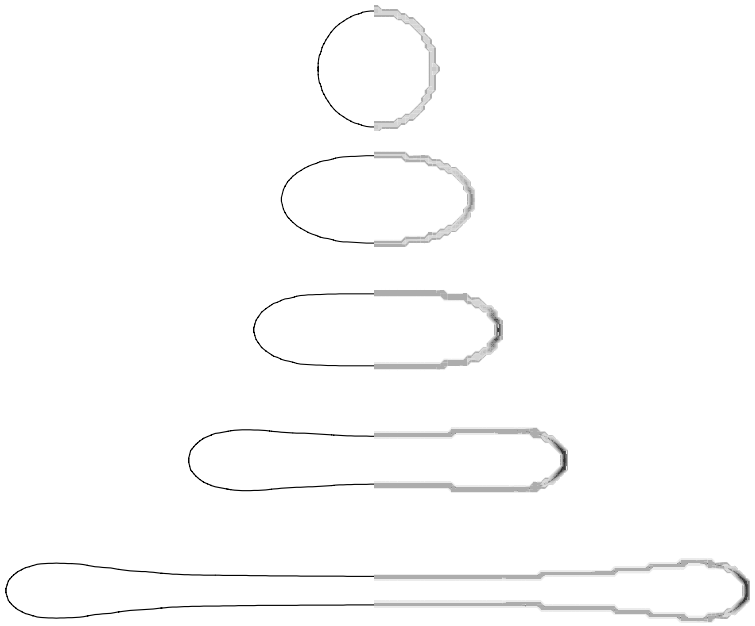

Fig. 23. The surfactant concentration contours. The contours (right) are equally spaced every 0.25 units up to a concentration of 6 for the case shown in Fig. 22.

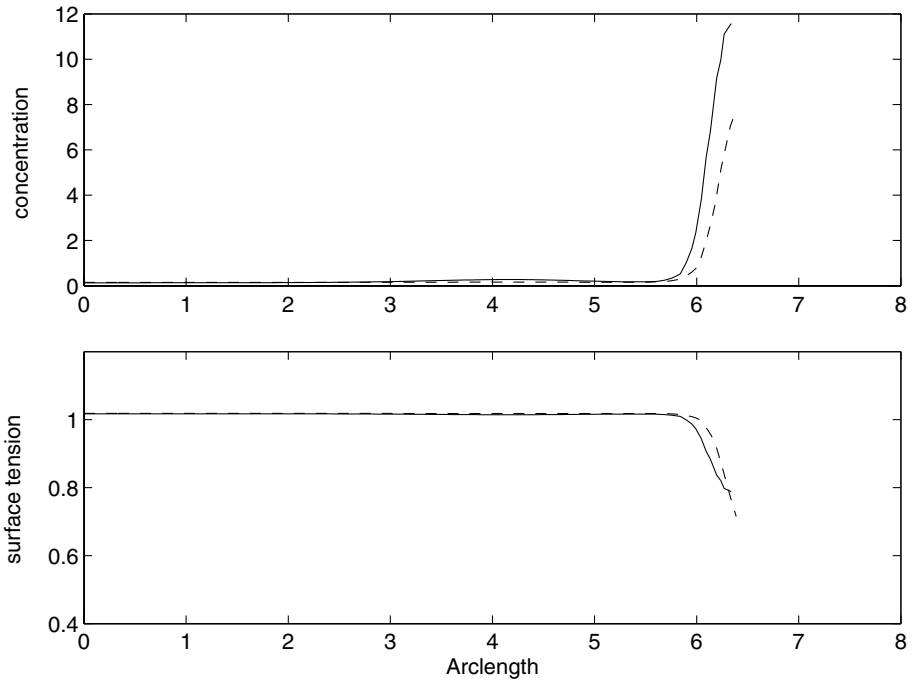

Fig. 24. The surfactant concentration (top) and surface tension (bottom) on a drop subjected to extension. The data correspond to the linear (solid) and nonlinear (dashed) equation of state for the final time shown in Fig. 22.

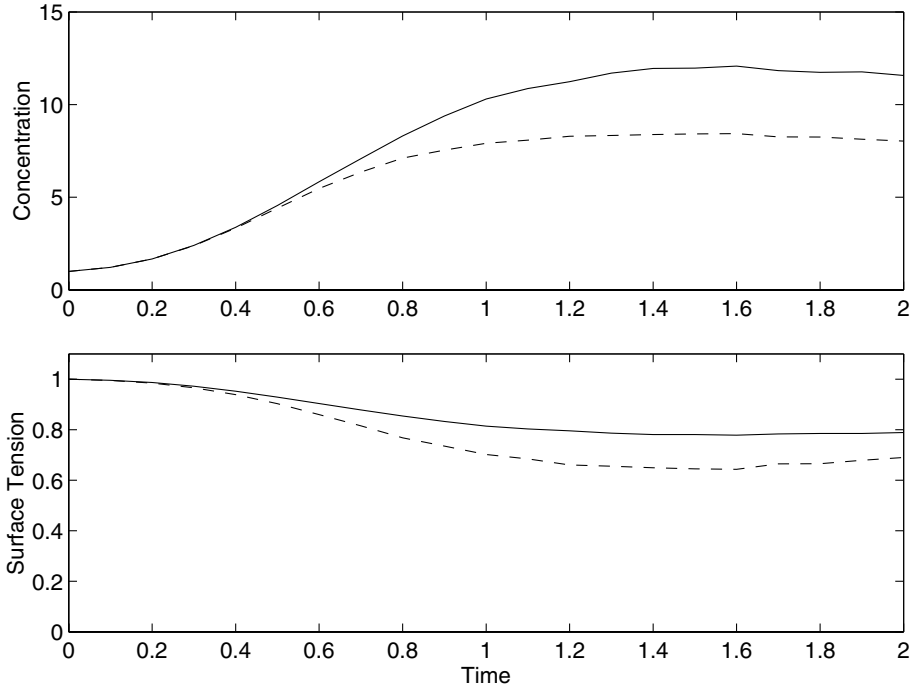

Fig. 25. The evolution of the surfactant concentration (top) and surface tension (bottom) at the drop tip. The data correspond to the linear (solid) and nonlinear (dashed) equation of state for the times shown in Fig. 22.

equation of state (solid) since Marangoni forces less strongly resist surfactant redistribution than when the nonlinear equation of state (dashed) is used. In spite of having a larger surfactant concentration, the drop using the linear equation of state has a larger surface tension (solid) near the drop tip than does the corresponding nonlinear case (dashed). Indeed as shown in Fig. 25, we find that at the drop tip the surfactant concentration is larger in the linear (solid) case while the surface tension is smaller for the nonlinear (dashed) case throughout the course of the simulation. This explains why in the nonlinear case, the drop stretches farther.

In Fig. 26, we consider the Marangoni and capillary forces for the drops from Fig. 22. The roughness in these plots is due to limited numerical resolution. In Fig. 26 (top), the maximum Maragoni force $\max|\nabla_s\sigma|$ is plotted as a function of time for the linear (solid) and nonlinear (dashed) equations of state. The maximum Marangoni force occurs a small distance behind the drop tip. The Marangoni force resists the redistribution of the surfactant to the drop tip and is much larger for the nonlinear case (dashed). The capillary force $|\sigma\kappa|$ at the drop tip is roughly comparable for the linear and nonlinear cases. For this surfactant coverage ($x = 0.1$ and $\beta = 0.02$), it appears that the the capillary force dominates the Marangoni force. This explains why the difference between the linear and nonlinear results is rather small. At higher coverages, the deviation between linear and nonlinear can be much bigger [62,9] and our preliminary results [62] indicate that the Marangoni and capillary force can balance when the nonlinear equation of state is used.

Finally, these simulations show that even though the initial surfactant distribution may be dilute (so that the linear and nonlinear equations of state nearly match initially), the surfactant distribution at the drop tips increasingly deviates from the dilute limit as the surfactant accumulates. This, together with the associated capillary and Marangoni forces, leads to the observed differences between results using the linear and nonlinear equations of state (see also [9]).

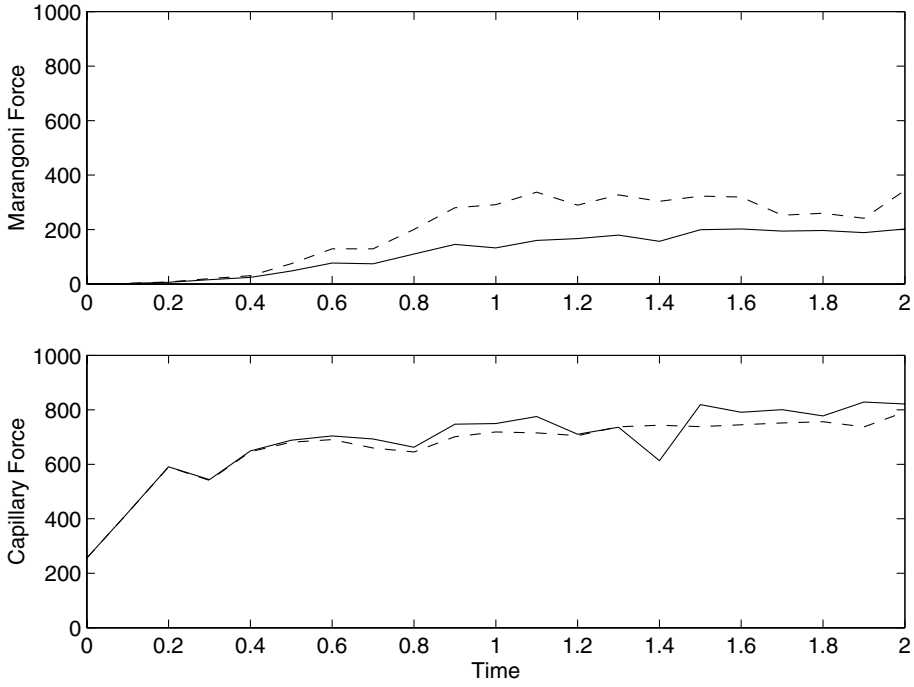

Fig. 26. The maximum Marangoni force (top) and the capillary force at the drop tip (bottom) for the two surfactant coverages. Data correspond to the results from Fig. 22. Nonlinear results (dashed) and linear results (solid).

4.7. Drop retraction

We now consider the retraction of the extended drops at the final time from Fig. 22 together with a case in which the surfactant coverage is increased. In the higher coverage case, the linear equation of state is used with $\beta = 0.06$ and as in Fig. 22, the initially spherical drop is subjected to the extensional flow until time $t = 2.0$. Because the surface tension is lower, the drop corresponding to the higher surfactant coverage deforms more than the lower coverage counterparts. The external flow is turned off and the capillary number is set to $Ca = 1.0$ to reflect the surface tension time scale. All other parameters are as in Fig. 22. The retraction of the drops due to surface tension is shown in Fig. 27. In this figure, the right half of the drop shows the greyscale contours of the surfactant concentration. As the drops retract, the surfactant-free drop pinches off first followed by those with surfactant. As the drop pinches off, two daughter drops (and tiny fragments) are produced. The central mass of fluid retracts, deforms and, in the case of $x = 0.1$, restabilizes to produce a nearly spherical drop that has a small oscillation due to the finite Reynolds number ($Re = 1$). In the case of $\beta = 0.06$, the central mass of fluid undergoes further pinchoff events to produce two additional satellite drops. Interestingly, at the lower coverage $x = 0.1$ (and $\beta = 0.02$) the final drop configurations are very similar even though the drop dynamics is a bit different.

As the drops retract, surfactant is slowly swept from the drop tip back towards the drop center. At early times, this is shown in Fig. 28 where the surfactant concentration (top) and surface tension (bottom) are plotted for the evolving drops using the linear (dashed) and the nonlinear (solid) equations of state for the lower coverage case $x = 0.1$ and $\beta = 0.02$. After the pinchoff, most of the surfactant remains with the two daughter drops; the central mass of fluid contains much less surfactant. Although it appears that some of the surfactant has left the interface, this is because only the $F = 0.5$ contour is plotted. An examination of

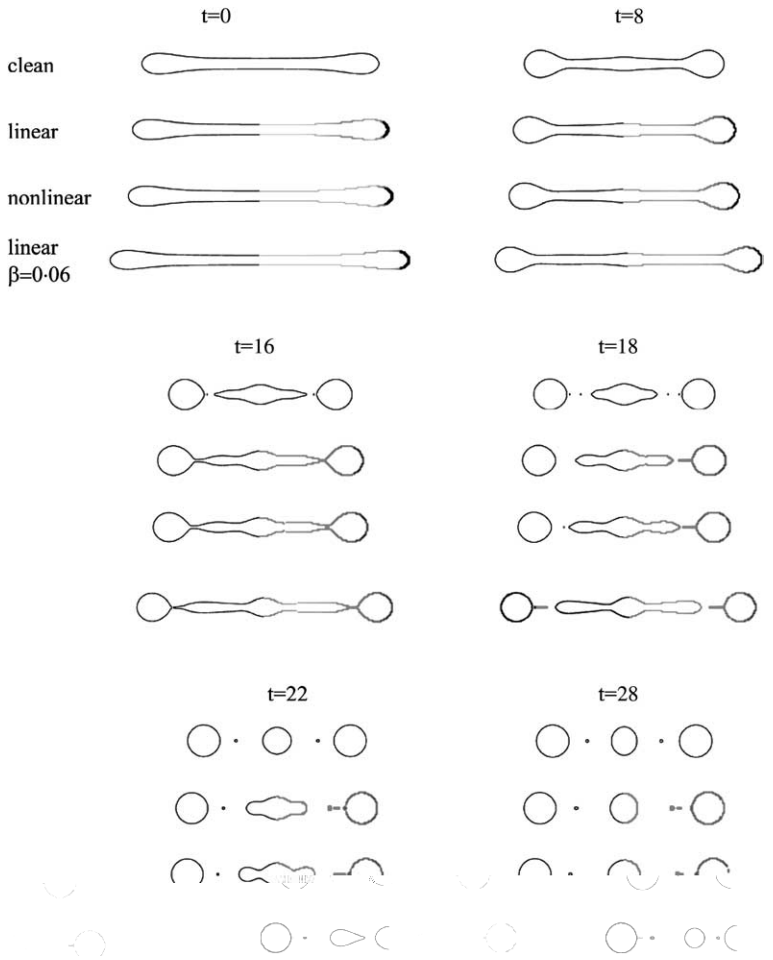

Fig. 27. The evolution of retracting droplets. The initial droplets and surfactant concentration correspond to the final time shown in Fig. 22 (the simulation with $\beta = 0.06$ is obtained analogously). Here, $Ca = 1.0$ and all other parameters as in those figures. The right half of the drops show the greyscale contours of the surfactant concentration ranging from 0 to 2.0.

the data show that the surfactant concentration is actually zero in regions where $F = 0$ or 1. As the central mass retracts and the daughter drops become more spherical, the surfactant redistributes reaching nearly uniform values. In the case of $\beta = 0.06$, the central drop contains slightly less surfactant than the smaller satellites.

5. Conclusions and future work

In this paper, we presented a volume of fluid method that accounts for an evolving surface distribution of insoluble surfactant and the associated Marangoni force in an axisymmetric geometry. The masses of the fluid components and of the surfactant are exactly conserved. An arbitrary equation of state relating the surfactant concentration to the surface tension may be used. A number of test cases were presented to validate the algorithm. Simulations of a drop in extensional flow, and its subsequent retraction and breakup

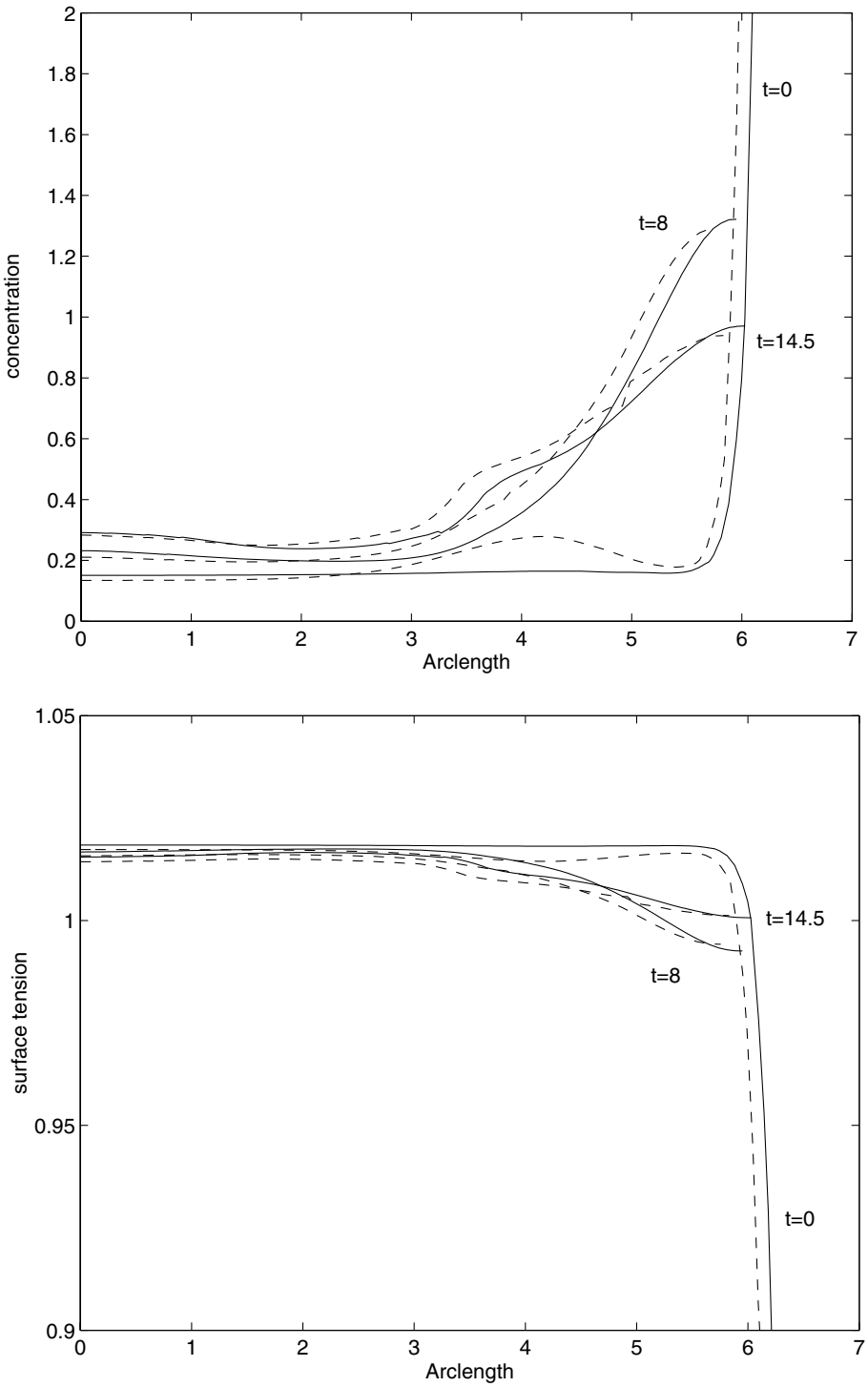

Fig. 28. The surfactant concentration (top) and the surface tension (bottom) for the drops in Fig. 27. Dashed: Linear equation of state ($\beta = 0.02$); Solid: Nonlinear equation of state ($x = 0.1$).

upon cessation of the external flow, were performed. Even when the initial surfactant distribution is dilute, we observed that increases in surfactant concentration locally (i.e. at the drop tips) can result in a local deviation from the dilute limit. We showed that this can lead to differences in effective surface tension, Marangoni forces and the associated drop dynamics between results using the linear and nonlinear equations of state.

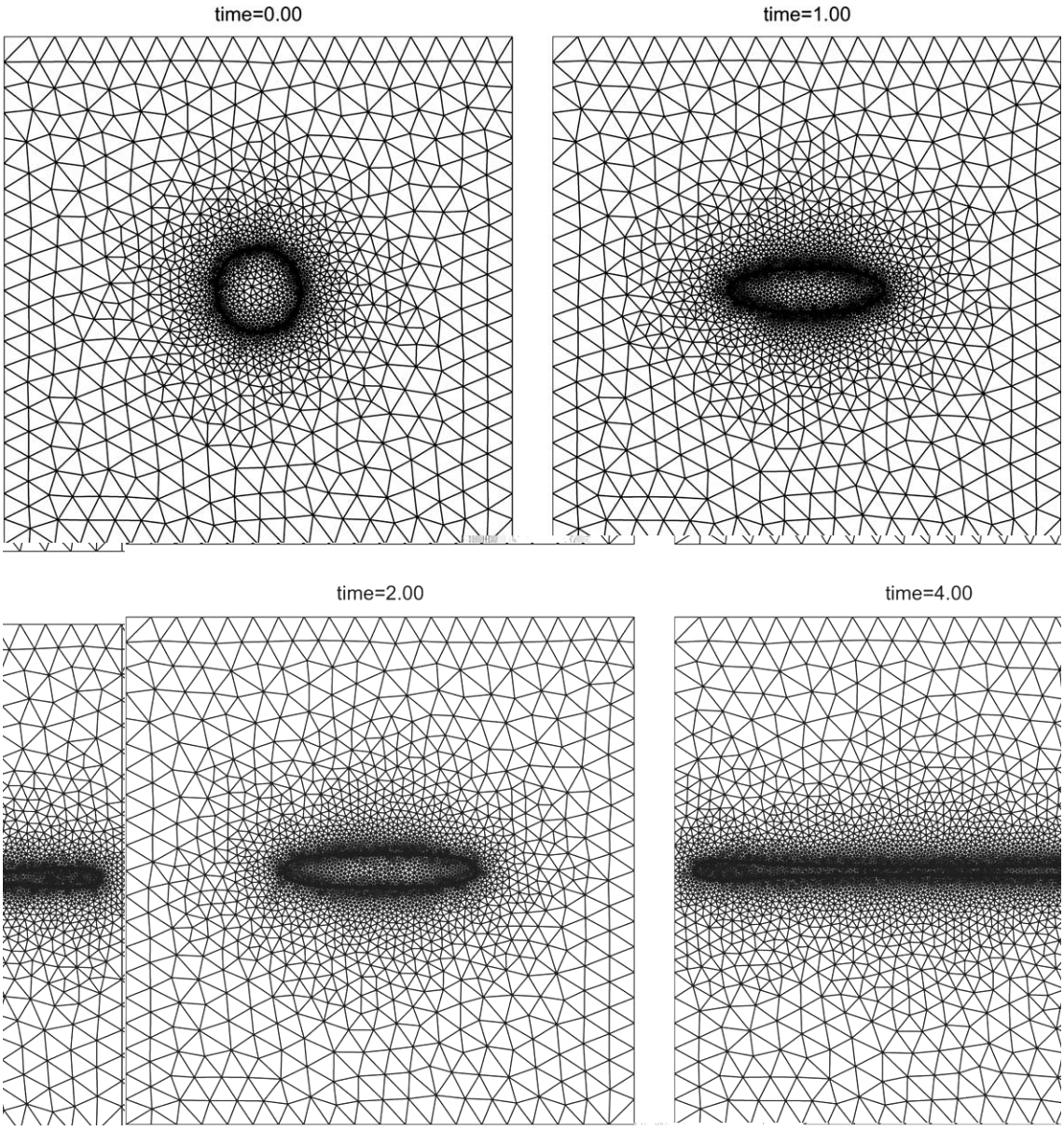

Fig. 29. Mesh adaptation in 2D drop extension.

There are numerous flow configurations we will simulate in the future, and several of these problems will be used to compare our results to experiments. Comparison is difficult since the total amount of surfactant on the interface generally cannot be measured, much less the surfactant distribution. However, our simulations can be used to determine such quantities a posteriori by finding the parameters needed to match experimental results. Such results can be very useful to the experimentalist. For example, we will compare the velocity of a bubble rising under buoyancy, with and without surfactant, to experimental data. By matching the bubble velocity, we will then likely be able to predict the actual surfactant coverage and distribution in the experiment. In particular, we will simulate experiments by Zhang and Finch [69] which report the velocity of a buoyant bubble as a function of distance traveled after being released from rest for three surfactant concentrations and two bubble sizes. In another problem of interest, Hu et al. [70] quantify the deformation of a drop subjected to an extensional flow as a function of the capillary number and the average surface tension. They vary the surface tension by varying surfactant concentration. Thus, by matching the drop deformation in this experiment, we will also be able to predict the actual surfactant coverage and distribution along the drop.

There are several directions we will pursue in the future. To resolve the wide-ranging length and time scales inherent in interfacial flows with surfactants, we will implement adaptive mesh refinement. This is necessary to resolve, for example, very small secondary drops that may pinchoff from the ends of a primary drop in the presence of surfactant (tip streaming). We will adapt the mesh refinement algorithms developed by Zheng et al. [64] for level-set methods to a coupled level-set/volume-of-fluid method. In [64], a finite element implementation of the the level-set equations for low Reynolds number interfacial flows (without surfactant) was solved using an unstructured, adaptive triangulated mesh in 2D and an unstructured tetrahedral mesh in 3D. The mesh is adapted according to a node density function [65] such that the density of nodes is highest near the interface. In preliminary work, we have developed a 2D implementation of a coupled level-set/volume-of-fluid algorithm [66] for clean drops and an example simulation of a drop in extensional flow using this new algorithm is shown in Fig. 29. Observe that the mesh is highly refined near the interface and tracks the evolution of the interface throughout the domain.

In additional future work, we will link the volume fraction and interface area advection routines to create a higher-order, self-consistent interface reconstruction. We will also simulate the transport of soluble surfactant in the fluid bulk and transfer of surfactant between the bulk and the interface. Finally, the simulations will be generalized to 3D.

Acknowledgements

The authors thank Mike Siegel and especially Vittorio Cristini for helpful discussions concerning this work. The authors acknowledge the support of the Minnesota Supercomputer Institute and the Network and Academic Computing Services (NACS) at the University of California, Irvine. The first author thanks 3M Corp. for partial support. The second author thanks the National Science Foundation, Division of Mathematical Sciences and the Department of Energy, Basic Energy Sciences Division for partial support. The authors thank the Institute for Mathematics and its Applications at the University of Minnesota for hospitality.

Appendix A. Concentration evolution equation

In this appendix, we demonstrate that Eq. (5) for the surfactant concentration is equivalent to alternative formulations for incompressible given, for example, in [5]. For incompressible fluids,

$$-\underline{n}\cdot\nabla\underline{u}\cdot\underline{n} = \left(\underline{\underline{I}} - \underline{n}\underline{n}\right) : \nabla\underline{u}, \tag{A.1}$$

where $\underline{\underline{I}}$ is the identity tensor. Next, observe that

$$(\underline{\underline{I}} - \underline{n}\underline{n}) : \nabla\underline{u} = \nabla_S \cdot \underline{u}_S + \kappa u_n, \tag{A.2}$$

where $\underline{u}_S = (\underline{\underline{I}} - \underline{n}\underline{n})\underline{u}$ is the projection of the velocity in the tangential directions and $u_n = \underline{u}\cdot\underline{n}$ is the normal velocity. Using these in Eq. (5), we obtain

$$\frac{\partial\Gamma}{\partial t} + \underline{u}\cdot\nabla\Gamma = \frac{1}{Pe_S}\nabla_S^2\Gamma - \Gamma\nabla_S\underline{u}_S - \Gamma\kappa u_n, \tag{A.3}$$

which is the form of the surfactant equation given in [5]. This also shows that Eq. (5) is well defined and that $\underline{n}\cdot\nabla\underline{u}\cdot\underline{n}$ is continuous across the interface.

Interestingly, from Eqs. (A.1) and (A.2) it follows that the normal component of the strain tensor is also continuous across the interface, i.e.

$$[[\underline{n}\cdot(\nabla\underline{u} + \nabla\underline{u}^T)\cdot\underline{n}]]_\Sigma = 0 \tag{A.4}$$

for any viscosity ratio. Further, it can be seen that the classical jump conditions for the normal stress across the interface (e.g. [2]) can be written as

$$-[[p]]_\Sigma + (1-\lambda)\underline{n}\cdot\nabla\underline{u}\cdot\underline{n} = -\kappa, \tag{A.5}$$

$$[[\eta(\underline{\underline{I}} - \underline{n}\underline{n})(\nabla\underline{u} + \nabla\underline{u}^T)\cdot\underline{n}]]_\Sigma = \nabla_S\sigma, \tag{A.6}$$

where η is equal to one in fluid 1 and to λ in fluid 2.

Appendix B. Surface stress

In this appendix, we derive the form of the total surface tension stress, given in Eq. (46), acting along an interface segment from a point A to a point B. The total stress is given by

$$\underline{F_{AB}} = -\int_A^B \left(\sigma\kappa\underline{n} - \frac{\partial\sigma}{\partial s}\underline{s}\right) r\,\mathrm{d}s, \tag{B.1}$$

where s is the arclength in the r–z plane, the curvature $\kappa = \kappa_{rz} + (n_r/r)$, κ_{rz} is the (2D) curvature in the r–z plane and n_r is the r-component of the normal vector to the interface. Using the Frenet formulas in the r–z plane,

$$\frac{\partial}{\partial s}\underline{s} = -\kappa_{rz}\underline{n} \quad \text{and} \quad \frac{\partial}{\partial s}\underline{n} = \kappa_{rz}\underline{s}, \tag{B.2}$$

we find that

$$\underline{F_{AB}} = \int_A^B \left[\frac{\partial}{\partial s}(r\sigma\underline{s}) - \sigma\left(\frac{\partial r}{\partial s}\underline{s} + n_r\underline{n}\right)\right]\mathrm{d}s. \tag{B.3}$$

But, a straightforward calculation shows that $\underline{r} = \frac{\partial r}{\partial s}\underline{s} + n_r\underline{n}$. Thus Eq. (B.3) becomes

$$\underline{F_{AB}} = (r_B\sigma_B\underline{s} - r_A\sigma_A\underline{s}) - \underline{r}\int_A^B \sigma\,\mathrm{d}s, \tag{B.4}$$

as claimed in Eq. (46).

References

[1] R.A. De Bruijn, Tipstreaming of drops in simple shear flows, Chem. Eng. Sci. 48 (1993) 277–284.
[2] R. Defay, I. Priogine, Surface Tension and Adsorption, Wiley, New York, 1966.
[3] D.I. Colliasand, R.K. Prudhomme, Diagnostic techniques of mixing effectiveness: the effect of shear and elongation in drop production in mixing tanks, Chem. Eng. Sci. 47 (1992) 1401–1410.
[4] H.P. Grace, Dispersion phenomena in high viscosity immiscible fluid systems and application of static mixers as dispersion devices in such systems, Chem. Eng. Commun. 14 (1982) 225–277.
[5] H.A. Stone, A simple derivation of the time-dependent convective–diffusion equation for surfactant transport along a deforming interface, Phys. Fluids A 2 (1990) 111.
[6] H. Wong, D. Rumschitzki, C. Maldarelli, On the surfactant mass balance at a deforming fluid interface, Phys. Fluids 8 (1996) 3203–3204.
[7] H.A. Stone, L.G. Leal, The effects of surfactants on drop deformation and breakup, J. Fluid Mech. 222 (1990) 161–186.
[8] W.J. Milliken, H.A. Stone, L.G. Leal, The effect of surfactant on transient motion of Newtonian drops, Phys. Fluids A 5 (1993) 69–79.
[9] Y. Pawar, K.J. Stebe, Marangoni effects on drop deformation in an extensional flow: the role of surfactant physical chemistry. I. Insoluble surfactants, Phys. Fluids 8 (1996) 1738–1751.
[10] C.D. Eggleton, Y.P. Pawar, K.J. Stebe, Insoluble surfactants on a drop in an extensional flow: a generalization of the stagnated surface limit to deforming interfaces, J. Fluid Mech. 385 (1999) 79–99.
[11] C.D. Eggleton, T.-M. Tsai, K.J. Stebe, Tip streaming from a drop in the presence of surfactants, Phys. Rev. Lett. 87 (2001) 048302.
[12] X. Li, C. Pozrikidis, The effect of surfactants on drop deformation and on the rheology of dilute emulsions in Stokes flow, J. Fluid Mech. 341 (1997) 165–194.
[13] S. Yon, C. Pozrikidis, A finite-volume/boundary-element method for flow past interfaces in the presence of surfactants, with application to shear flow past a viscous drop, Comput. Fluids 27 (1998) 879–902.
[14] W.J. Milliken, L.G. Leal, The influence of surfactant on the deformation and breakup of a viscous drop: the effect of surfactant solubility, J. Colloid Interface Sci. 166 (1994) 275–285.
[15] H. Zhou, V. Cristini, J. Lowengrub, C. W. Macosko, 3D adaptive finite-element simulations of deformable drops with soluble surfactant: pair interactions and coalescence. Phys. Fluids, submitted.
[16] Y.-J. Jan, G. Tryggvason, Computational studies of contaminated bubbles, in: I. Sahin, G. Tryggvason (Eds.), Proceedings of a Symposium on the Dynamics of Bubbles and Vorticity Near Free Surfaces, ASME, 1991, p. 46.
[17] H.D. Ceniceros, The effects of surfactants on the formation and evolution of capillary waves, Phys. Fluids 15 (2003) 245.
[18] J.U. Brackbill, D.B. Kothe, C. Zemach, A continuum method for modeling surface tension, J. Comput. Phys. 100 (1992) 335.
[19] J. Glimm, M.J. Graham, J. Grove, X.L. Li, T.M. Smith, D. Tan, F. Tangerman, Q. Zhang, Front tracking in two and three dimensions, Comput. Math. Appl. 35 (1998) 1.
[20] G. Tryggvason, B. Bunner, A. Esmaeeli, D. Juric, N. Al-Rawahi, W. Tauber, J. Han, S. Nas, Y.J. Jan, A front tracking method for the computations of multiphase flow, J. Comput. Phys. 169 (2001) 708.
[21] D.J. Torres, J.U. Brackbill, The point-set method: front tracking without connectivity, J. Comput. Phys. 165 (2000) 620.
[22] A. Shin, D. Juric, Modeling three-dimensional multiphase flow using a level contour reconstruction method for front tracking without connectivity, J. Comput. Phys. 180 (2002) 427–470.
[23] S. Osher, R. Fedkiw, Level set methods: an overview and some recent results, J. Comput. Phys. 169 (2001) 463.
[24] M. Sussman, P. Smereka, S. Osher, A level-set approach for computing solutions to incompressible two-phase flow, J. Comput. Phys. 114 (1994) 146.
[25] M. Sussman, A. Almgren, J. Bell, P. Colella, L. Howell, M. Welcome, An adaptive level set approach for incompressible two-phase flows, J. Comput. Phys. 148 (1999) 81.
[26] Z. Li, R. Leveque, Immersed interface methods for Stokes flow with elastic boundaries or surface tension, SIAM J. Sci. Comput. 18 (1997) 709.
[27] L. Lee, R. Leveque, An immmersed interface method for incompressible Navier–Stokes equations, SIAM J. Sci. Comput. 25 (2003) 832.
[28] D. Jacqmin, Calculation of two-phase Navier–Stokes flows using phase-field modeling, J. Comput. Phys. 55 (1999) 96.
[29] D. Anderson, G.B. McFadden, A.A. Wheeler, Diffuse interface methods in fluid mechanics, Ann. Rev. Fluid Mech. 30 (1998) 139.
[30] H. Lee, J. Lowengrub, J. Goodman, Modeling pinchoff and reconnection in a Hele–Shaw cell: I. The models and their calibration, Phys. Fluids 14 (2002) 492–513.
[31] H. Lee, J. Lowengrub, J. Goodman, Modeling pinchoff and reconnection in a Hele–Shaw cell: II. Analysis and simulation in the nonlinear regime, Phys. Fluids 14 (2002) 514–545.
[32] M. Verschueren, F.N. van de Vosseand, H.E.H. Meijer, Diffuse-interface modeling of thermocapillary flow instabilities in a Hele–Shaw cell, J. Fluid Mech. 434 (2001) 153.

[33] J.-S Kim, K. Kang, J. Lowengrub, Conservative multigrid methods for Cahn–Hilliard fluids, J. Comput. Phys. 193 (2004) 511–543.
[34] Y.Y. Renardy, M. Renardy, V. Cristini, A new volume-of-fluid formulation for surfactants and simulations of drop deformation under shear at a low viscosity ratio, Eur. J. Mech. B 21 (2002) 49–59.
[35] A.J. James, M.K. Smith, A. Glezer, Vibration induced drop atomization and the numerical simulation of low-frequency single-droplet ejection, J. Fluid Mech. 476 (2003) 29–62.
[36] M. Renardy, Y. Renardy, J. Li, Numerical simulation of moving contact line problems using a volume-of-fluid method, J. Comput. Phys. 171 (2001) 243–263.
[37] R. Scardovelli, S. Zaleski, Direct numerical simulation of free surface and interfacial flow, Ann. Rev. Fluid Mech. 31 (1999) 576.
[38] J. Li, Y. Renardy, Numerical study of flows of two immiscible liquids at low Reynolds number, SIAM Rev. 42 (2000) 417–439.
[39] Y. Renardy, V. Cristini, Effect of inertia on drop breakup under shear, Phys. Fluids 13 (2001) 7–13.
[40] E.G. Puckett, A. Almgren, J. Bell, D.L. Marcus, W.G. Rider, A high-order projection method for tracking fluid interfaces in variable density incompressible flows, J. Comput. Phys. 130 (1997) 269.
[41] Y. Renardy, M. Renardy, PROST: a parabolic reconstruction of surface tension for the volume-of-fluid method, J. Comput. Phys. 183 (2002) 400–421.
[42] C.W. Hirt, B.D. Nichols, Volume of fluid (VOF) method for the dynamics of free boundaries, J. Comput. Phys. 39 (1981) 201–225.
[43] M. Sussman, E.G. Puckett, A coupled level-set and volume-of-fluid method for computing 3D and axisymmetric incompressible two-phase flows, J. Comput. Phys. 162 (2000) 301–337.
[44] A. Bourlioux, A coupled level-set volume-of-fluid method for tracking material interfaces, in: Proceedings of the 6th Annual Int. Symposium on Computational Fluid Dynamics, Lake Tahoe, CA, 1995.
[45] M. Sussman, A second order coupled level-set and volume-of-fluid method for computing growth and collapse of vapor bubbles, J. Comput. Phys. 187 (2003) 110.
[46] R. Fedkiw, T. Aslam, B. Merriman, S. Osher, A nonoscillatory Eulerian approach to interfaces in multimaterials flows (the ghost fluid method), J. Comput. Phys. 152 (1999) 423.
[47] H.S. Udaykumar, L. Tran, D.M. Belk, K.J. Vanden, An Eulerian method for computation of multimaterial impact with ENO shock-capturing and sharp interfaces, J. Comput. Phys. 186 (2003) 136–177.
[48] T. Hou, Z. Li, S. Osher, H. Zhao, A hybrid method for moving interface problems with applications to Hele–Shaw flow, J. Comput. Phys. 134 (1997) 457.
[49] B.T. Helenbrook, L. Martinelli, C.K. Law, A numerical method for solving incompressible flow problems with a surface of discontinuity, J. Comput. Phys. 148 (1999) 366.
[50] G.P. Sasmal, J.I. Hochstein, Marangoni convection with a curved and deforming free surface in a cavity, J. Fluids Eng. 116 (1994) 557–582.
[51] M.A. Drumright-Clarke, Y. Renardy, The effect of insoluble surfactant at dilute concentration on drop breakup under shear with inertia, Phys. Fluids 16 (2004) 14–21.
[52] J.-J. Xu, H.-K. Zhao, An Eularian formulation for solving partial differential equations along a moving interface, J. Sci. Comput. 19 (2003) 573–594.
[53] G.K. Batchelor, An Introduction to Fluid Dynamics, Cambridge University Press, New York, 1967.
[54] D.B. Kothe, R.C. Mjolsness, M.D. Torrey, RIPPLE: A computer program for incompressible flows with free surfaces, Los Alamos National Lab Report LA-12007-MS, 1991.
[55] B.D. Nichols, C.W. Hirt, R.S. Hotchkiss, SOLA-VOF: A solution algorithm for transient fluid flow with multiple free boundaries, Los Alamos National Lab Report LA-8355, 1980.
[56] R. Scardovelli, S. Zaleski, Direct numerical simulation of free-surface and interfacial flow, Ann. Rev. Fluid Mech. 31 (1999) 567–603.
[57] F.H. Harlow, J.E. Welch, Numerical calculation of time-dependent viscous incompressible flow of fluid with free surface, Phys. Fluids 8 (1965) 2182–2189.
[58] J.A. Meijerink, H.A. van der Vorst, Guidelines for the usage of incomplete decompositions in solving sets of linear equations as they occur in practical problems, J. Comput. Phys. 44 (1981) 134–155.
[59] A.J. James, Vibration induced droplet ejection, Ph.D. Thesis, Georgia Institute of Technology, 2000.
[60] E.G. Puckett, A.S. Almgren, J.B. Bell, D.L. Marcus, W.J. Rider, A high-order projection method for tracking fluid interfaces in variable density incompressible flows, J. Comput. Phys. 130 (1997) 269–282.
[61] D.B. Kothe, W.J. Rider, S.J. Mosso, J.S. Brock, J.I. Hochstein, Volume tracking of interfaces having surface tension in two and three dimensions, in: Proceedings of the 34th Aerospace Sciences Meeting & Exhibit, January 15–18, 1996, Reno, NV, AIAA Report 96-0859, 1996.
[62] A. James, J. Lowengrub, in preparation.
[63] M. Siegel, 2000, private communication.

[64] V. Cristini, J. Lowengrub, Z. Zheng, A. Anderson, Adaptive remeshing algorithms for unstructured meshes: application to interface capturing simulations of multiphase flows, J. Comput. Phys., submitted.
[65] V. Cristini, J. Blawzdziewicz, M. Loewenberg, An adaptive mesh algorithm for evolving surfaces: simulations of drop break-up and coalescence, J. Comput. Phys. 169 (2001) 345–463.
[66] X. Yang, A. James, J. Lowengrub, X. Zheng, V. Cristini, An adaptive coupled level-set/volume-of-fluid method, in preparation.
[67] J. Li, Calcul d'interface affine par morceauz (piecewise linear interface calculation), C. R. Acad. Sci. Paris., Ser. IIb (Paris) 320 (1995) 391–396.
[68] R. Scardovelli, S. Zaleski, Interface reconstruction with least-square fit and split Eulerian–Lagrangian advection, Int. J. Numer. Methods Fluids 41 (2003) 251–274.
[69] Y. Zhang, J.A. Finch, A note on single bubble motion in surfactant solutions, J. Fluid Mech. 429 (2001) 63–66.
[70] Y.T. Hu, D.J. Pine, L.G. Leal, Drop deformation, breakup, and coalescence with compatibilizer, Phys. Fluids 12 (2000) 484–489.